Roles of dynamical symmetry breaking in driving oblate-prolate transitions of atomic clusters

Yurie Oka, Tomohiro Yanao, and Wang Sang Koon

Citation: The Journal of Chemical Physics **142**, 134105 (2015); doi: 10.1063/1.4915928
View online: http://dx.doi.org/10.1063/1.4915928
View Table of Contents: http://scitation.aip.org/content/aip/journal/jcp/142/13?ver=pdfcov
Published by the AIP Publishing

Roles of dynamical symmetry breaking in driving oblate-prolate transitions of atomic clusters

Yurie Oka,[1,a)] Tomohiro Yanao,[1,b)] and Wang Sang Koon[2,c)]
[1]*Department of Applied Mechanics and Aerospace Engineering, Waseda University, Tokyo 169-8555, Japan*
[2]*Control and Dynamical Systems, California Institute of Technology, Pasadena, California 91125, USA*

(Received 22 January 2015; accepted 11 March 2015; published online 2 April 2015)

This paper explores the driving mechanisms for structural transitions of atomic clusters between oblate and prolate isomers. We employ the hyperspherical coordinates to investigate structural dynamics of a seven-atom cluster at a coarse-grained level in terms of the dynamics of three gyration radii and three principal axes, which characterize overall mass distributions of the cluster. Dynamics of gyration radii is governed by two kinds of forces. One is the potential force originating from the interactions between atoms. The other is the dynamical forces called the internal centrifugal forces, which originate from twisting and shearing motions of the system. The internal centrifugal force arising from twisting motions has an effect of breaking the symmetry between two gyration radii. As a result, in an oblate isomer, activation of the internal centrifugal force that has the effect of breaking the symmetry between the two largest gyration radii is crucial in triggering structural transitions into prolate isomers. In a prolate isomer, on the other hand, activation of the internal centrifugal force that has the effect of breaking the symmetry between the two smallest gyration radii is crucial in triggering structural transitions into oblate isomers. Activation of a twisting motion that switches the movement patterns of three principal axes is also important for the onset of structural transitions between oblate and prolate isomers. Based on these trigger mechanisms, we finally show that selective activations of specific gyration radii and twisting motions, depending on the isomer of the cluster, can effectively induce structural transitions of the cluster. The results presented here could provide further insights into the control of molecular reactions. © *2015 AIP Publishing LLC.* [http://dx.doi.org/10.1063/1.4915928]

I. INTRODUCTION

Structural transitions of atomic clusters are the subject of significant interest in modern chemical physics.[1–21] For decades, there has been extensive progress in the understanding of structures and dynamics of atomic clusters from the viewpoints of energy landscapes,[1–4] phase transitions,[5–10] transition rates,[11–14] saddle crossing dynamics,[15–17] and rotational effects.[18–21] Structures and dynamics of atomic clusters can also provide many insights into the mechanisms for collective motions of even more complex and higher-order systems including molecular clusters[22,23] and self-organized nano-structures.[24–31] It is thereby of archetypal importance to explore the fundamental mechanisms for structural transitions of atomic clusters.

Since collective motions of molecular systems often involve a large number of degrees of freedom, coarse-graining and reduction of dimensionality[32,33] are useful for the understanding of their mechanisms. Because of the coherent nature of collective motions, one can generally expect that the actual number of essential degrees of freedom in collective motions, which can also be referred to as collective variables or reaction coordinates, is not large. It is thereby an important issue of modern chemical physics to identify such small number of essential degrees of freedom. The methods of reaction path Hamiltonian,[34] transition path sampling,[35,36] and string methods[37,38] construct reaction coordinates in configuration space based on potential energy topographies, path action, and free energy topographies, respectively, in many typical examples. For more complex reactions with multiple equilibria and multiple transition states, the path sampling methods that do not require reaction coordinates but rather highlight the networks of local equilibria and transition states are effective.[39–42] These methods are often combined with statistical mechanics and make it possible to estimate reaction rates. Complementarily to these methods, there exist phase-space methods,[43–47] which highlight the roles of invariant manifolds in phase space and are suitable to the study of nonlinear dynamical effects and non-statistical effects.

Motivated by the recent progress in the understanding of collective variables and their dynamics, the present study examines three gyration radii and associated three principal axes as candidates for essential degrees of freedom that dominate structural transitions. This is based on the observation that structural transitions of molecular systems often accompany significant changes in overall mass distributions, which are precisely characterized by the three gyration radii and associated three principal axes of a system. An advantage of using gyration radii and principal axes as candidates for essential degrees of freedom is that these variables are inherent

[a)]Electronic mail: ok-yu@fuji.waseda.jp
[b)]Author to whom correspondence should be addressed. Electronic mail: yanao@waseda.jp
[c)]Electronic mail: koon@cds.caltech.edu

in any molecular systems and their equations of motion are in a common form for any many-atom systems. Therefore, dynamics of gyration radii and principal axes can provide a common footing for the understanding of collective motions of molecular systems. Moreover, gyration radii and principal axes could be useful for the study of transformations of symmetry of molecular mass distributions, which are often essential characteristics of structural transitions of self-organized nano-structures. For example, typical structures of atomic clusters,[1–4] fullerenes,[24–26] viral capsids,[27,28] and colloid clusters[29–31] often possess oblate, prolate, or spherical mass distributions. It is noteworthy that the roles of prolate-oblate oscillations attract interest in the rearrangement and fragmentation dynamics of fullerenes from the viewpoint of intramolecular vibrational energy redistribution.[26]

For the systematic understanding of the dynamics of three gyration radii and three principal axes of molecules, the hyperspherical coordinates that refer to the principal-axis frame,[48–58] i.e., the principal-axis hyperspherical coordinates, are remarkably suitable. Recently, the authors have been utilizing these hyperspherical coordinates with the framework of geometric mechanics,[59–67] which gives a rigorous treatment of the coupling between molecular vibrations and rotations, to study structural transitions of molecular systems.[68–72] The hyperspherical coordinates consist of three gyration radii and $3n - 9$ hyperangular degrees of freedom. While the three gyration radii characterize the instantaneous mass distributions of the system along the three instantaneous principal axes, the $3n - 9$ hyperangular degrees of freedom characterize the internal shape changes. Three of the hyperangular degrees of freedom correspond to twisting motions, and the remaining $3n - 12$ hyperangular degrees of freedom correspond to shearing motions.[71] Activations of the twisting and shearing motions induce dynamical forces called the internal centrifugal forces.[70,71] The internal centrifugal force originating from the twisting motions has an effect of breaking the symmetry between two of the gyration radii. While the potential forces generally play the role of restoring the symmetry of mass distribution of a molecule, the internal centrifugal forces can be a driving force for structural transitions by breaking the symmetry of molecular mass distribution.

The present study pays particular attention to the roles of this symmetry breaking effect of the internal centrifugal force in structural transitions of a seven-atom Lennard-Jones cluster between oblate and prolate isomers. Since the two largest gyration radii are nearly equal in an oblate isomer, we expect that activation of the internal centrifugal force that has the effect of breaking the symmetry between the two largest gyration radii can trigger structural transitions in an oblate isomer. Likewise, since the two smallest gyration radii are nearly equal in a prolate isomer, we expect that activation of the internal centrifugal force that has the effect of breaking the symmetry between the two smallest gyration radii can trigger structural transitions in a prolate isomer. The first part of the present study is devoted to confirm these initial expectations based on theoretical and numerical investigations.

After confirming the above expectations, we characterize the trigger mechanisms in terms of energy transfer among internal degrees of freedom of the cluster. This is motivated by the recent progress in the experimental techniques of femtosecond activation,[73] spectroscopy,[74] bond-selective chemistry,[75] and computational studies,[76,77] which have revealed the existence of certain pathways of energy transfer even in chaotic dynamics of complex molecular systems. Moreover, recent studies[75,77–79] have suggested that one can utilize these pathways of energy transfer to induce molecular reactions by selectively activating specific degrees of freedom. Since the hyperspherical coordinates give a concise and universal expression for the kinetic energy of many-atom systems,[48–58,70,71] our present approach is indeed suitable to the study of energy transfer among internal degrees of freedom. By taking this advantage, we identify characteristic pathways of energy transfer that are responsible for the onset of structural transitions of the cluster between oblate and prolate isomers. We finally show that selective activations of specific gyration radii and twisting motions, depending on the isomer of the cluster, can effectively induce structural transitions of the cluster.

This paper is organized as follows. In Sec. II, we introduce the model of a seven-atom Lennard-Jones cluster and summarize the framework of the hyperspherical coordinates. In Sec. III, we apply the hyperspherical coordinates to the structural transition dynamics of the cluster between oblate and prolate isomers, and characterize their internal driving mechanisms. We highlight the roles of specific internal centrifugal forces that break the symmetry of mass distributions of the oblate and prolate isomers. Based on these driving mechanisms, in Sec. IV, we examine the possibility to induce structural transitions of the cluster by selectively activating the specific hyperspherical degrees of freedom. In Sec. V, we summarize the results and discuss future directions of research.

II. HYPERSPHERICAL DESCRIPTION OF SEVEN-ATOM CLUSTERS

A. Model cluster

Model of the present study is an atomic cluster composed of seven identical atoms. The system is in vacuum and is isolated. The constituent atoms of the cluster interact through the pairwise Lennard-Jones potential. Therefore, the system is called the LJ_7 cluster. Dimensionless Hamiltonian of the LJ_7 cluster is given by

$$\tilde{\mathcal{H}} = \frac{\mathcal{H}}{\varepsilon} = \frac{1}{2}\sum_{i=1}^{7} \boldsymbol{p}_i \cdot \boldsymbol{p}_i + 4\sum_{i<j}\left[\left(\frac{1}{r_{ij}}\right)^{12} - \left(\frac{1}{r_{ij}}\right)^{6}\right], \quad (1)$$

where $\boldsymbol{p}_i = \dot{\boldsymbol{r}}_i$, and $\boldsymbol{r}_i$ is the three-dimensional position vector of atom i ($i = 1, \ldots, 7$), and r_{ij} is the distance between atom i and atom j. The dot over $\boldsymbol{r}_i$ represents the time derivative. All quantities on the right-hand side of Eq. (1) are dimensionless. See Refs. 13 and 14, for example, for the derivation of the dimensionless Hamiltonian in Eq. (1). All the masses of atoms can be regarded as unity in the dimensionless Hamiltonian. The second term on the right-hand side of Eq. (1) is the Lennard-Jones potential. $\tilde{\mathcal{H}}$ is the dimensionless Hamiltonian and the parameter ε represents the depth of the Lennard-Jones potential. In this study, the parameter ε serves as the unit of energy. The model can be regarded as an Ar_7-like cluster when ε

$= 1.67 \times 10^{-21}$ J. In the present study, all physical quantities are presented in dimensionless units unless otherwise noted. Throughout the present study, we investigate the Hamiltonian dynamics of the LJ_7 cluster, where the total energy of the system is a constant of motion. The typical value of total energy is $E = -13.5\varepsilon$ unless otherwise noted in the present study. We restrict ourselves to the systems whose total angular momentum is zero throughout the present study.

The LJ_7 cluster has four geometrically distinct isomers called the pentagonal bipyramid (PBP), the capped octahedron (COCT), the tricapped tetrahedron (IST), and the bicapped trigonal bipyramid (SKEW) in the order of potential energy[1,2,12,13] as shown in Fig. 1. When the total energy of the cluster is sufficiently low as in the solid-like phase, the cluster undergoes small-amplitude vibrations around one of the four isomers. When the total energy is sufficiently high as in the liquid-like phase, the cluster undergoes structural transitions among these four isomers. It is known that there exists a coexistence phase between the solid-like and liquid-like phases. These phase behaviors were scrutinized in Refs. 5–7.

B. Gyration radii and principal axes as collective variables

We introduce here the three gyration radii and the three principal axes for the study of the LJ_7 cluster. These variables serve as the collective (or coarse) variables that characterize the structural transitions of the LJ_7 cluster. See Ref. 70 for a six-atom cluster.

We begin with an n-atom system whose constituent atoms have masses m_i $(i = 1,\ldots,n)$ for generality. Note, however, that for our dimensionless system of Eq. (1), all masses are equal to unity, $m_i = 1$ $(i = 1,\ldots,7)$, and the position vectors $\{\boldsymbol{r}_i\}$ are dimensionless. Use of the mass-weighted Jacobi vectors,

$$\boldsymbol{\rho}_i = \sqrt{\mu_i}\left(\frac{\sum_{k=1}^{i} m_k \boldsymbol{r}_k}{\sum_{k=1}^{i} m_k} - \boldsymbol{r}_{i+1}\right) \quad (i = 1,\ldots,n-1), \tag{2}$$

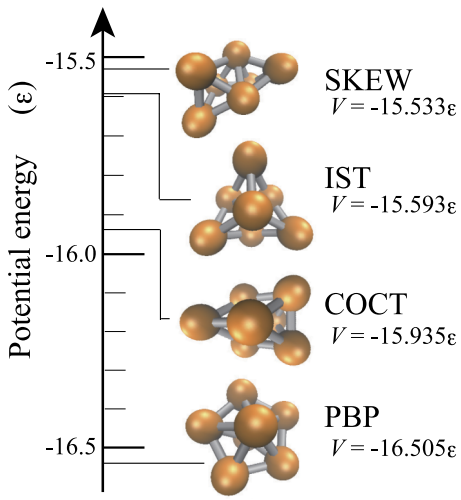

FIG. 1. Four isomers of the LJ_7 cluster, the pentagonal bipyramid (PBP), the capped octahedron (COCT), the tricapped tetrahedron (IST), and the bicapped trigonal bipyramid (SKEW). Potential energies at the equilibrium points are shown for the respective isomers.

where μ_i are the reduced masses defined as

$$\mu_i = \frac{m_{i+1}\sum_{k=1}^{i} m_k}{\sum_{k=1}^{i+1} m_k} \quad (i = 1,\ldots,n-1), \tag{3}$$

eliminates the overall translational degrees of freedom of the system. We then apply the singular-value decomposition to the $3 \times (n-1)$-dimensional matrix W consisting of the Jacobi vectors

$$\mathsf{W} = \begin{pmatrix} \boldsymbol{\rho}_1 & \cdots & \boldsymbol{\rho}_{n-1} \end{pmatrix}, \tag{4}$$

to obtain the decomposition of the matrix W into the product of three matrices as

$$\mathsf{W} = \mathsf{RNU}^T, \tag{5}$$

where

$$\mathsf{R} = \begin{pmatrix} \boldsymbol{e}_1 & \boldsymbol{e}_2 & \boldsymbol{e}_3 \end{pmatrix}, \tag{6}$$

$$\mathsf{N} = \begin{pmatrix} a_1 & 0 & 0 & 0 & \cdots & 0 \\ 0 & a_2 & 0 & 0 & \cdots & 0 \\ 0 & 0 & a_3 & 0 & \cdots & 0 \end{pmatrix}, \tag{7}$$

$$\mathsf{U} = \begin{pmatrix} \boldsymbol{u}_1 & \boldsymbol{u}_2 & \boldsymbol{u}_3 & \boldsymbol{u}_4 & \cdots & \boldsymbol{u}_{n-1} \end{pmatrix}. \tag{8}$$

In Eq. (5) and hereafter, the symbol T on a matrix indicates the matrix transpose. The matrix R is a 3×3 orthogonal matrix (SO(3)), whose column vectors, $\boldsymbol{e}_1$, $\boldsymbol{e}_2$, $\boldsymbol{e}_3$, are orthogonal and normalized. These vectors, $\boldsymbol{e}_1$, $\boldsymbol{e}_2$, $\boldsymbol{e}_3$, coincide with the principal axes of moment of inertial tensor of the system about center of mass. The matrix N is a $3 \times (n-1)$ diagonal matrix. The diagonal elements (singular values), a_1, a_2, a_3, are the gyration radii. These variables are non-negative and ordered as

$$a_1 \geq a_2 \geq a_3 \geq 0. \tag{9}$$

Although there are many alternative definitions for the Jacobi vectors, the values of gyration radii are independent of the definitions of Jacobi vectors. The three gyration radii are related to the three principal moments of inertia about the center of mass of the system, M_1, M_2, and M_3 $(M_3 \geq M_2 \geq M_1 \geq 0)$, as

$$M_1 = a_2^2 + a_3^2, \quad M_2 = a_3^2 + a_1^2, \quad M_3 = a_1^2 + a_2^2. \tag{10}$$

The matrix U is an $(n-1) \times (n-1)$ orthogonal matrix (SO($n-1$)), whose column vectors, $\boldsymbol{u}_1,\ldots,\boldsymbol{u}_{n-1}$, are orthogonal and normalized. In the principal-axis hyperspherical coordinates, the principal-axis frame R specifies the instantaneous orientation of the system, while N and U determine the size and shape of the system. Gyration radii, a_1, a_2, and a_3, are the measure of the mass-weighted length of the system along the respective principal axes. In other words, they characterize the *mass distribution* of the system.

Table I summarizes the values of the three gyration radii (dimensionless) for the four isomers of the LJ_7 cluster at the

TABLE I. Gyration radii of the four isomers of the LJ_7 cluster at equilibrium points.

Isomer	PBP	COCT	IST	SKEW
a_1	1.51	1.69	1.53	1.86
a_2	1.51	1.12	1.53	1.12
a_3	0.81	1.12	0.94	1.02
Mass distribution	Oblate	Prolate	Oblate	Near prolate

respective equilibrium points. These four isomers are classified into two groups in terms of their mass-distributions. Specifically, PBP and IST are classified as *oblate*, where the two largest gyration radii are equal, $a_1 = a_2$, at the equilibrium points. COCT is classified as *prolate*, where the two smallest gyration radii are equal, $a_2 = a_3$, at the equilibrium point. SKEW can be classified as near prolate since a_2 and a_3 are nearly equal, while the value of a_1 is largely different.

In this manner, three gyration radii take the characteristic values at the respective equilibrium points. It is thereby possible to characterize the four isomers of the LJ_7 cluster in terms of the values of gyration radii, a_1, a_2, a_3, at a coarse-grained level in the dynamics. Fig. 2 shows the projections of a trajectory of the cluster at total energy $E = -13.5\varepsilon$ in the a_1-a_2-a_3-space onto the (a) a_1-a_2 plane and onto the (b) a_3-a_2 plane. In Fig. 2, the trajectory is plotted with squares (red), crosses (blue), diamonds (green), and triangles (orange) when the cluster is in the PBP, COCT, IST, and SKEW isomers, respectively. Here, we have attributed every point on the trajectory to one of the four isomers uniquely by following the steepest descent path on the potential energy surface.[1] That is, we solved the first order equations,

$$\frac{d\boldsymbol{r}_i}{d\tau} = -\frac{\partial V}{\partial \boldsymbol{r}_i}, \quad (i = 1, \ldots, 7), \tag{11}$$

at each point along the trajectory until the system reaches one of the four minima of the potential energy V, where the parameter τ is arbitrary.

From Fig. 2, we see that the three gyration radii distinguish the four isomers fairly well. In particular, the three gyration radii clearly distinguish the oblate isomers (PBP, IST) and the prolate isomers (COCT, SKEW). Thus, the a_1-a_2 plane and the a_3-a_2 plane will serve as the fundamental planes to characterize the mechanisms for structural transitions in Sec. III.

In addition to the three gyration radii, the corresponding three principal axes $(\boldsymbol{e}_1, \boldsymbol{e}_2, \boldsymbol{e}_3)$ defined in Eq. (6) are of interest. Fig. 3 shows the typical movement patterns (time evolutions) of the three principal axes in the three-dimensional physical space when the cluster is in the (a) PBP, (b) COCT, (c) IST, and (d) SKEW isomers, respectively. All the principal axes are orthogonal and normalized to unity based on Eq. (6), and only the "heads" of the axis vectors $(\pm\boldsymbol{e}_1, \pm\boldsymbol{e}_2, \pm\boldsymbol{e}_3)$ are plotted with different symbols (different colors). Since there is no distinction in the signs of principal axes, we plotted the "heads" of both $\boldsymbol{e}_i$ and $-\boldsymbol{e}_i$ $(i = 1, 2, 3)$ at every instant. Base points of these vectors coincide with the center of mass of the LJ_7 cluster and with the origin of the space-fixed frame, which is represented by the frame labeled as x, y, z in each of Figs. 3(a)–3(d). Thus, all the plot points in Figs. 3(a)–3(d) lie on the surface of a unit sphere. It should be noted that even though the total

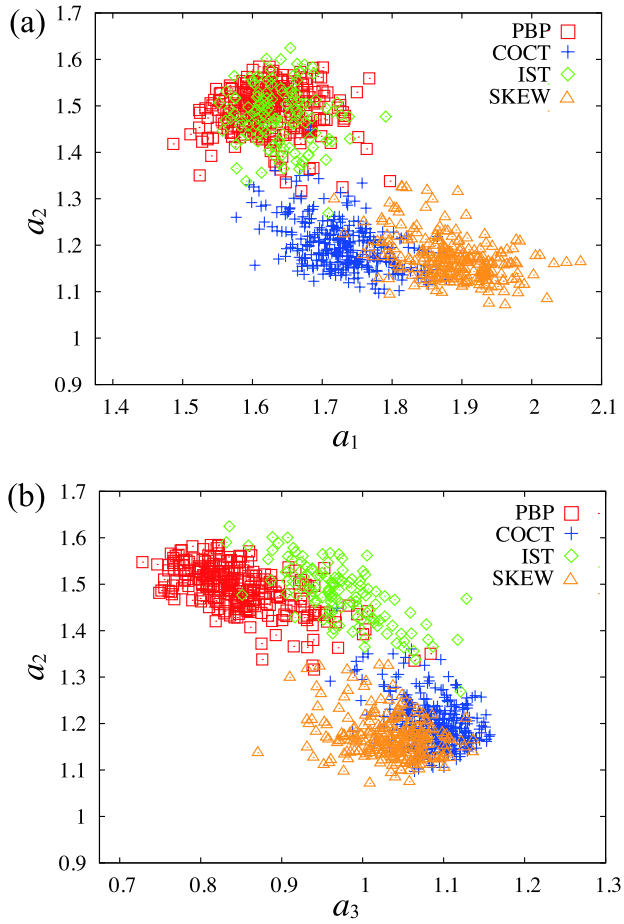

FIG. 2. Projections of a trajectory of total energy $E = -13.5\varepsilon$ onto the planes of gyration radii (collective variables), (a) a_1-a_2 plane and (b) a_3-a_2 plane. Squares (red), crosses (blue), diamonds (green), and triangles (orange) represent the portions of the trajectory in the PBP, COCT, IST, and SKEW isomers, respectively.

angular momentum of the cluster is zero, the three principal axes move in the physical space as a result of internal dynamics (vibrations) of the cluster.

We see from Figs. 3(a) and 3(c) that, in PBP and IST, which are oblate isomers, the third principal axis $\boldsymbol{e}_3$ is almost fixed in the space, while the first $\boldsymbol{e}_1$ and the second $\boldsymbol{e}_2$ principal axes couple each other and corotate in the plane perpendicular to the third principal axis forming the "ring." In COCT and SKEW, which are prolate and nearly prolate isomers, the first principal axis $\boldsymbol{e}_1$ is almost fixed in the space, while the second $\boldsymbol{e}_2$ and the third $\boldsymbol{e}_3$ principal axes couple each other and corotate in the plane perpendicular to the first principal axis forming the "ring" as we see from Figs. 3(b) and 3(d). These results indicate that transitions between the different movement patterns of principal axes are also important for the structural transitions between oblate and prolate isomers in addition to the changes in the values of gyration radii shown in Fig. 2. In the end of Subsection II C, we will present an account for the mechanisms for the characteristic movement patterns of principal axes observed in Fig. 3.

C. Kinetic energy and hyperspherical modes

We summarize here the expression for the internal kinetic energy of an n-atom system in terms of the hyperspherical

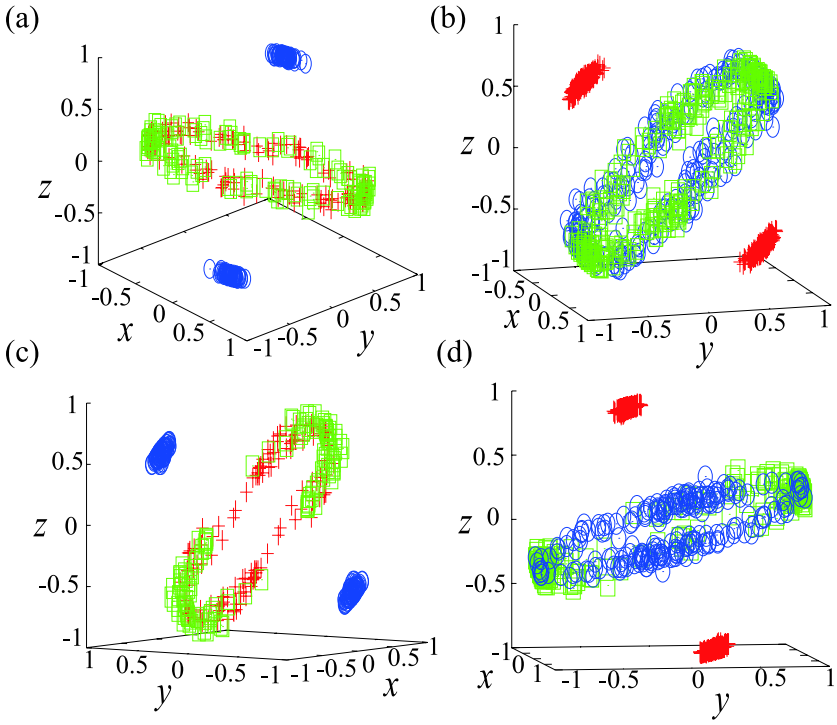

FIG. 3. Typical movement patterns of three principal axes $(\boldsymbol{e}_1, \boldsymbol{e}_2, \boldsymbol{e}_3)$ of the LJ_7 cluster about the center of mass in the three-dimensional physical space when the cluster is in the (a) PBP, (b) COCT, (c) IST, (d) SKEW isomers, respectively. At every instant, only the "heads" of both vectors $\boldsymbol{e}_i$ and $-\boldsymbol{e}_i$ $(i = 1,2,3)$ are plotted. Base points of these vectors coincide with the center of mass of the LJ_7 cluster and with the origin of the space-fixed frame, which is represented by the frame labeled as x, y, z in each of (a)-(d). Crosses (red), squares (green), and circles (blue) represent the "heads" of the first $(\pm\boldsymbol{e}_1)$, second $(\pm\boldsymbol{e}_2)$, and third $(\pm\boldsymbol{e}_3)$ principal axes, respectively.

coordinates and the physical meanings of the hyperspherical variables for the LJ_7 cluster.

Internal kinetic energy of an n-atom system is given by[70]

$$K = \frac{1}{2}\left(\dot{a}_1^2 + \dot{a}_2^2 + \dot{a}_3^2\right) + \frac{\left(a_1^2 - a_2^2\right)^2}{2\left(a_1^2 + a_2^2\right)}\omega_{12}^2 + \frac{\left(a_2^2 - a_3^2\right)^2}{2\left(a_2^2 + a_3^2\right)}\omega_{23}^2 + \frac{\left(a_3^2 - a_1^2\right)^2}{2\left(a_3^2 + a_1^2\right)}\omega_{31}^2 + \frac{1}{2}a_1^2\sum_{k=4}^{n-1}\gamma_{1k}^2 + \frac{1}{2}a_2^2\sum_{k=4}^{n-1}\gamma_{2k}^2 + \frac{1}{2}a_3^2\sum_{k=4}^{n-1}\gamma_{3k}^2, \quad (12)$$

where $\{\omega_{ij}\}$ and $\{\gamma_{ik}\}$ are the quasivelocities defined by

$$\dot{\boldsymbol{u}}_i \cdot \boldsymbol{u}_j = -\boldsymbol{u}_i \cdot \dot{\boldsymbol{u}}_j \equiv \omega_{ij} \quad (i,j = 1,2,3, \;\; i \neq j), \quad (13)$$

$$\dot{\boldsymbol{u}}_i \cdot \boldsymbol{u}_k = -\boldsymbol{u}_i \cdot \dot{\boldsymbol{u}}_k \equiv \gamma_{ik} \quad (i = 1,2,3, \;\; k = 4,\ldots,n-1). \quad (14)$$

The vectors $\{\boldsymbol{u}_i\}$ are the $(n-1)$-dimensional vectors defined as the columns of the matrix U in Eq. (5). The quasivelocities $\{\omega_{ij}\}$ are anti-symmetric with respect to the exchange of the subscripts as $\omega_{ij} = -\omega_{ji}$. Both $\{\omega_{ij}\}$ and $\{\gamma_{ik}\}$ are the components of the $(n-1)\times(n-1)$ anti-symmetric matrix $\mathsf{U}^T\dot{\mathsf{U}}$, which is essentially an *internal* angular velocity associated with shape changes of the system.

One can see the physical meanings of the quasivelocities in Eq. (12) by expanding the velocity vector $\dot{\mathsf{W}}$, which is the time derivative of Eq. (4), under the conditions of zero total angular momentum as

$$\dot{\mathsf{W}} = \sum_{i=1}^{3}\dot{a}_i\mathsf{V}_{a_i} + \sum_{ij=12,23,31}\omega_{ij}\mathsf{V}_{\omega_{ij}} + \sum_{i=1}^{3}\sum_{k=4}^{n-1}\gamma_{ik}\mathsf{V}_{\gamma_{ik}}, \quad (15)$$

where $\{\mathsf{V}_{a_i}\}$, $\{\mathsf{V}_{\omega_{ij}}\}$, and $\{\mathsf{V}_{\gamma_{ik}}\}$ are $3\times(n-1)$ matrices. See Ref. 71 for the explicit expressions for these matrices. The components of V_{a_i}, $\mathsf{V}_{\omega_{ij}}$, and $\mathsf{V}_{\gamma_{ik}}$ represent the components of tangent vectors of the $(3n-3)$-dimensional space of Jacobi vectors $\{\boldsymbol{\rho}_i | i = 1,\ldots,n-1\}$. Therefore, the components of V_{a_i}, $\mathsf{V}_{\omega_{ij}}$, and $\mathsf{V}_{\gamma_{ik}}$ can be transformed into the tangent vectors of the $3n$-dimensional space of position vectors $\{\boldsymbol{r}_i | i = 1,\ldots,n\}$ through the inverse transformation of Eq. (2). In this manner, V_{a_i}, $\mathsf{V}_{\omega_{ij}}$, and $\mathsf{V}_{\gamma_{ik}}$ are visualized as vectors in the three-dimensional physical space and are interpreted as the *gyration-radius modes*, *twisting modes*, and *shearing modes*, respectively, based on their physical meanings.[71] All of these modes are called the hyperspherical modes. Note that the hyperspherical modes are based only on the kinetic energy, Eq. (12), and are independent of the potential energy of the system. This is a major difference from the standard normal modes. For other sets of hyperspherical modes also based only on the kinetic energy and defined, in the long run, via the singular value decomposition of the position matrices, see Refs. 55–58. These hyperspherical modes are applied to structural relaxations of NO-doped Kr crystals.[80,81]

Figure 4 shows the respective hyperspherical modes defined in Eq. (15) for the PBP and COCT isomers of the LJ_7 cluster. Figs. 4(a)–4(c) and Figs. 4(A)–4(C) show the gyration-radius modes, i.e., a_1-,a_2-, and a_3-modes for the PBP and COCT isomers. It is clearly seen that the gyration-radius modes represent inflations of the system along the three principal axes, respectively. Figs. 4(d)–4(f) and Figs. 4(D)–4(F) show the twisting modes, i.e., ω_{12}-, ω_{23}-, and ω_{31}-modes. Figs. 4(g1)–4(i3) and Figs. 4(G1)–4(I3) represent shearing modes, i.e., γ_{ik}-modes $(i = 1,2,3, k = 4,5,6)$. The shearing mode γ_{ik} represents shearing motions of the system along ith principal axis.

In this manner, one can determine the hyperspherical modes for an arbitrary configuration of an n-atom system as long as the singular value decomposition Eq. (5) is well defined. It should be noted that the singular value decomposition Eq. (5) is not unique exactly at the equilibrium points of PBP and COCT since degeneracy among singular values, $a_1 = a_2$ or $a_2 = a_3$, occurs at each of these equilibrium points.

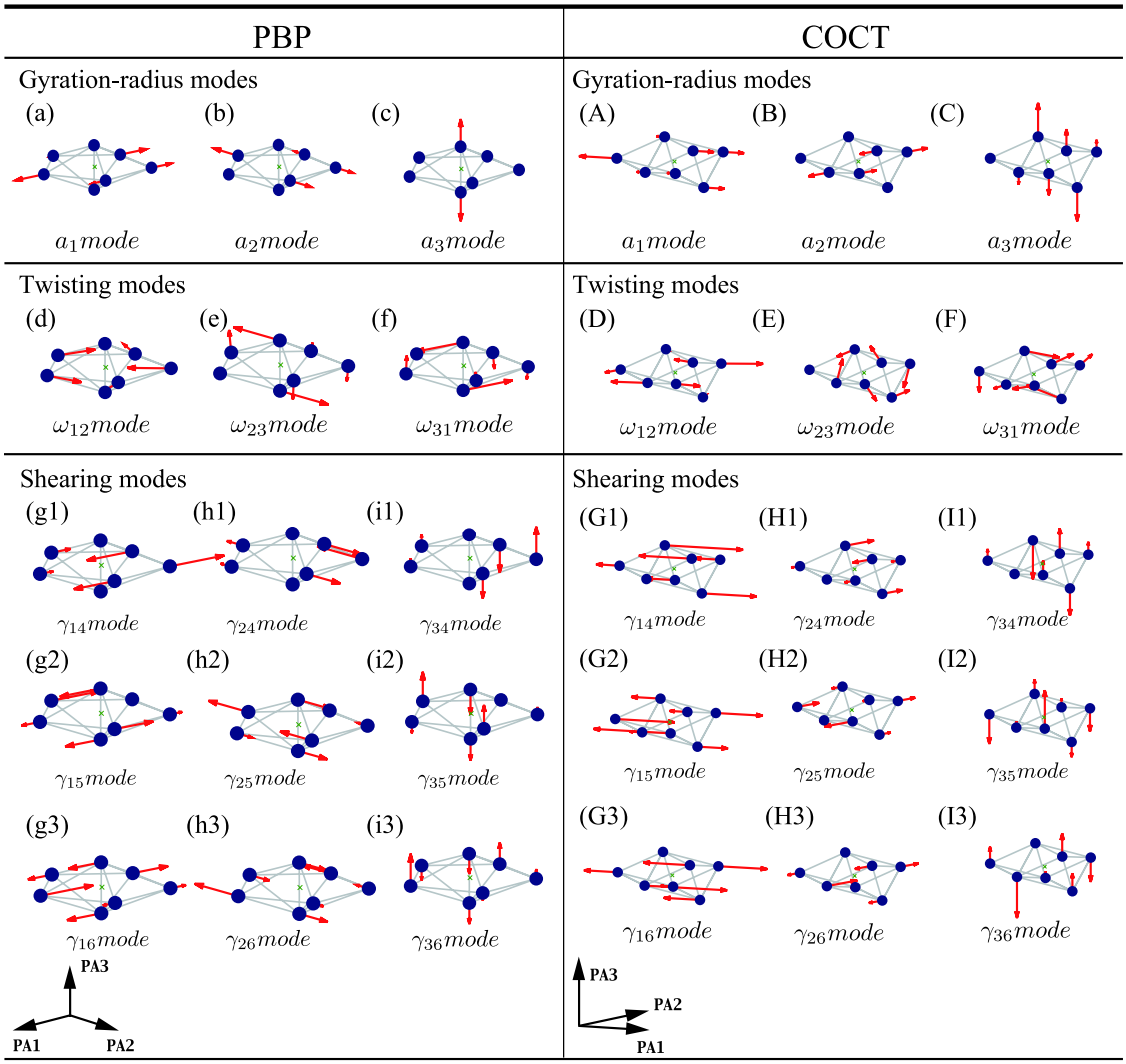

FIG. 4. Schematic representations of the 15 hyperspherical modes for the PBP ((a)-(i3)) and COCT ((A)-(I3)) isomers of the LJ_7 cluster. (a)–(c) and (A)–(C) represent the gyration-radius modes, i.e., a_1-, a_2-, and a_3-modes. (d)-(f) and (d′)-(f′) represent the twisting modes, i.e., ω_{12}-, ω_{23}-, and ω_{31}-modes, respectively. (g1)-(i3) and (G1)-(I3) represent shearing modes, i.e., γ_{ik}-modes ($i = 1, 2, 3, k = 4, 5, 6$), respectively. The triplets of axes labeled as PA1, PA2, and PA3 at the bottom represent the directionality of three principal axes for the shown configurations of PBP and COCT.

Therefore, in Fig. 4, we have slightly deformed the structure of the cluster out of the equilibrium points of PBP and COCT to avoid the degeneracy conditions $a_1 = a_2$ and $a_2 = a_3$, respectively.

The three quasi-velocities ω_{12}, ω_{23}, and ω_{31} of the twisting modes are related to the three components of the angular velocity of the principal-axis frame, Ω_{12}, Ω_{23}, and Ω_{31}, under the conditions of vanishing total angular momentum as[71]

$$\Omega_{12} = \frac{2a_1a_2}{a_1^2 + a_2^2}\omega_{12}, \tag{16}$$

$$\Omega_{23} = \frac{2a_2a_3}{a_2^2 + a_3^2}\omega_{23}, \tag{17}$$

$$\Omega_{31} = \frac{2a_3a_1}{a_3^2 + a_1^2}\omega_{31}. \tag{18}$$

Thus, the twisting modes are directly related to the movements of the three principal axes under the conditions of vanishing total angular momentum.

Based on the relationships of Eqs. (16)–(18), we can give an account for the characteristic movements of the three principal axes in the oblate and prolate isomers shown in Fig. 3. Suppose that the total kinetic energy of the cluster is roughly equipartitioned among all the hyperspherical degrees of freedom when the cluster is vibrating in each of the four isomers. This means that the statistical average of each term of Eq. (12) is roughly the same in each isomer. This is a reasonable assumption when the cluster is in equilibrium. In this situation, Eq. (12) indicates that ω_{12}^2 can be very large when the cluster is in an oblate isomer, where $a_1 \approx a_2$. This large ω_{12}^2 indicates an extensive coupling between the first and the second principal axes, according to Eq. (16). This explains why the first and the second principal axes couple strongly and corotate in the oblate isomers such as PBP and IST as shown in Figs. 3(a) and 3(c). In the same way, Eq. (12) indicates that ω_{23}^2 can be very large when the cluster is in a prolate isomer, where $a_2 \approx a_3$. This large ω_{23}^2 leads to a strong coupling between the second and the third principal axes, according to Eq. (17). This explains why the second and the third principal axes couple strongly

and corotate in prolate isomers such as COCT and SKEW as shown in Figs. 3(b) and 3(d).

D. Equations of motion for gyration radii

In order to understand the dynamics of three gyration radii, we summarize here classical equations of motion for gyration radii for systems with zero total angular momentum in vacuum. Lagrangian for the n-atom system with vanishing total angular momentum is given by $\mathcal{L} = K - V$, where K is the internal kinetic energy given in Eq. (12) and V is a potential function. In our model of LJ_7 cluster, V is a function only of the internal degrees of freedom. The Euler-Lagrange equations for the gyration radii of an n-atom system are in the form of[70]

$$\ddot{a}_1 = f_{\mathrm{ic},1} + f_{\mathrm{pot},1}, \tag{19}$$

$$\ddot{a}_2 = f_{\mathrm{ic},2} + f_{\mathrm{pot},2}, \tag{20}$$

$$\ddot{a}_3 = f_{\mathrm{ic},3} + f_{\mathrm{pot},3}, \tag{21}$$

where $f_{\mathrm{ic},i}$ $(i = 1,2,3)$ are

$$f_{\mathrm{ic},1} = \Gamma_{12}\omega_{12}^2 + \Gamma_{13}\omega_{31}^2 + a_1 \sum_{k=4}^{n-1} \gamma_{1k}^2, \tag{22}$$

$$f_{\mathrm{ic},2} = \Gamma_{21}\omega_{12}^2 + \Gamma_{23}\omega_{23}^2 + a_2 \sum_{k=4}^{n-1} \gamma_{2k}^2, \tag{23}$$

$$f_{\mathrm{ic},3} = \Gamma_{31}\omega_{31}^2 + \Gamma_{32}\omega_{23}^2 + a_3 \sum_{k=4}^{n-1} \gamma_{3k}^2, \tag{24}$$

and the coefficients are

$$\Gamma_{ij} = \frac{a_i \left(a_i^2 + 3a_j^2\right)\left(a_i^2 - a_j^2\right)}{\left(a_i^2 + a_j^2\right)^2} \quad (i,j = 1,2,3,\ i \neq j). \tag{25}$$

The left hand sides of Eqs. (19)–(21) are accelerations of gyration radii. Therefore, the right hand sides are physically the forces that act on gyration radii. The second terms on the right hand sides of Eqs. (19)–(21), $f_{\mathrm{pot},i}$ $(i = 1,2,3)$, represent the potential forces, which are expressed as the gradient of the potential function as

$$f_{\mathrm{pot},i} = -\frac{\partial V}{\partial a_i} \quad (i = 1,2,3). \tag{26}$$

These are potential forces on gyration radii and generally play the role of restoring mass distribution of each isomer.

The first terms on the right hand sides of Eqs. (19)–(21) represent a *kinematic force* that originates from the dynamical coupling of gyration radii with the twisting and shearing modes introduced in Subsection II C. All of these kinematic force terms are quadratic in the quasivelocity components, ω_{ij} and γ_{ik}, as we see from Eqs. (22)–(24). Therefore, these terms essentially represent the *internal centrifugal forces* arising from twisting and shearing motions of the system.

It should be noted that the mass metric components for $\dot{a}_1^2, \dot{a}_2^2$, and $\dot{a}_3^2$ are all equal to unity as we see from Eq. (12). This means that the space of gyration radii as shown in Fig. 2 is *Euclidean* even though the $(3n-6)$-dimensional full internal space of the n-atom system is non-Euclidean. Therefore, it is convenient to introduce three-dimensional vectors of the internal centrifugal force $\boldsymbol{f}_{\mathrm{ic}}$ and the potential force $\boldsymbol{f}_{\mathrm{pot}}$ as

$$\boldsymbol{f}_{\mathrm{ic}} = (f_{\mathrm{ic},1}, f_{\mathrm{ic},2}, f_{\mathrm{ic},3}), \tag{27}$$

$$\boldsymbol{f}_{\mathrm{pot}} = (f_{\mathrm{pot},1}, f_{\mathrm{pot},2}, f_{\mathrm{pot},3}), \tag{28}$$

which can be regarded as the force fields in the three-dimensional space of gyration radii.

Roles of the internal centrifugal forces are of significant interest in Sec. III in the study of the driving forces for structural transitions of the cluster. We thus summarize here the physical properties of the internal centrifugal forces. We call the internal centrifugal force terms proportional to ω_{ij}^2 and γ_{ik}^2 in Eqs. (22)–(24) the *twist centrifugal forces* and the *shear centrifugal forces*, respectively. As for the twist centrifugal forces, it is convenient to regroup the force terms in Eqs. (22)–(24) into the following three-dimensional vector notations:

$$\boldsymbol{f}_{\omega_{12}} \equiv \left(\Gamma_{12}\omega_{12}^2,\ \Gamma_{21}\omega_{12}^2,\ 0\right), \tag{29}$$

$$\boldsymbol{f}_{\omega_{23}} \equiv \left(0,\ \Gamma_{23}\omega_{23}^2,\ \Gamma_{32}\omega_{23}^2\right), \tag{30}$$

$$\boldsymbol{f}_{\omega_{31}} \equiv \left(\Gamma_{13}\omega_{31}^2,\ 0,\ \Gamma_{31}\omega_{31}^2\right), \tag{31}$$

where $\boldsymbol{f}_{\omega_{ij}}$ $(ij = 12,23,31)$ can be regarded as the twist centrifugal force originating from the twisting mode ω_{ij}. Note that $\boldsymbol{f}_{\omega_{ij}}$ $(ij = 12,23,31)$ acts only on a_i and a_j.

Fig. 5 shows the projection of $\boldsymbol{f}_{\omega_{12}}$ on the a_1-a_2 plane for a fixed value of ω_{12} (Fig. 5(a)), and that of $\boldsymbol{f}_{\omega_{23}}$ on the a_3-a_2 plane for a fixed value of ω_{23} (Fig. 5(b)). The plotting ranges of Figs. 5(a) and 5(b) are adjusted to be similar to those of Figs. 2(a) and 2(b) for the sake of comparison. The dashed lines in Figs. 5(a) and 5(b) represent the equality between two gyration radii, $a_1 = a_2$ and $a_2 = a_3$, respectively. Since $a_1 \geq a_2 \geq a_3$ (Eq. (9)) by definition, the force fields in Figs. 5(a) and 5(b) are drawn only in the region where these inequality conditions are satisfied. Note that, in Fig. 5(b), a_3 is on the horizontal axis and a_2 is on the vertical axis in accordance with Fig. 2(b). From the force fields in Fig. 5, it is evident that the twist centrifugal force $\boldsymbol{f}_{\omega_{12}}$ has the effect of enlarging a_1 and decreasing a_2 (Fig. 5(a)), and the twist centrifugal force $\boldsymbol{f}_{\omega_{23}}$ has the effect of enlarging a_2 and decreasing a_3 (Fig. 5(b)). The twist centrifugal force $\boldsymbol{f}_{\omega_{31}}$ also has a similar property of enlarging a_1 and decreasing a_3. In short, the twist centrifugal force $\boldsymbol{f}_{\omega_{ij}}$ $(ij = 12,23,31)$ has the effect of breaking the equality between a_i and a_j, by enlarging the larger gyration radii and decreasing the smaller gyration radii. Since the three gyration radii represent the mass distributions among the three instantaneous principal axes, the above effects of the twist centrifugal forces are regarded as the *symmetry breaking effect* on the mass distribution of the system.

It is important to note that the force fields $\boldsymbol{f}_{\omega_{12}}$ and $\boldsymbol{f}_{\omega_{23}}$ shown in Figs. 5(a) and 5(b) are plotted for *fixed* values of ω_{12} and ω_{23}, respectively. In the actual dynamics of the cluster, magnitudes of the force fields can change dynamically depending on the magnitudes of ω_{12} and ω_{23}, respectively. That is, when $|\omega_{ij}|$ $(ij = 12,23,31)$ is large, i.e., the twisting mode ω_{ij} is active, the corresponding twist centrifugal force $\boldsymbol{f}_{\omega_{ij}}$ is also strong as Eqs. (29)–(31) indicate. In this manner, the dynamics of gyration radii and that of twisting modes are dynamically coupled. In fact, it is usually the case that the twist centrifugal force $\boldsymbol{f}_{\omega_{ij}}$ $(ij = 12,23,31)$ tends to be strong when the values of two gyration radii a_i and a_j are close to each other. This is

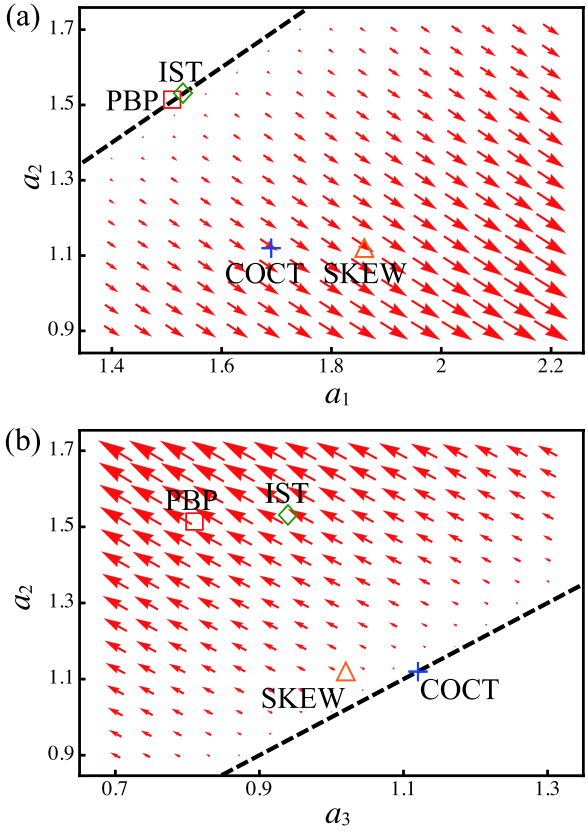

FIG. 5. Directionality of the twist centrifugal forces and the equilibrium points of isomers. (a) Projection of the force field of the twist centrifugal force $\boldsymbol{f}_{\omega_{12}}$ (Eq. (29)) on the a_1-a_2 plane for a fixed value of ω_{12}. (b) Projection of the force field of the twist centrifugal force $\boldsymbol{f}_{\omega_{23}}$ (Eq. (30)) on the a_3-a_2 plane for a fixed value of ω_{23}. The dashed lines in (a) and (b) represent the equalities between two gyration radii, $a_1 = a_2$ and $a_2 = a_3$, respectively. In each of (a) and (b), square (red), cross (blue), diamond (green), and triangle (orange) represent the locations of the equilibrium points (potential minima) of PBP, COCT, IST, and SKEW isomers of the LJ_7 cluster, respectively.

because when $a_i \approx a_j$, ω_{ij}^2 tends to be very large as noted in the end of Subsection II C.

The symmetry breaking effect of the twist centrifugal force is expected to play a crucial role in the onset of structural transitions of symmetric clusters, such as oblate, prolate, and spherical ones. In Figs. 5(a) and 5(b), square (red), cross (blue), diamond (green), and triangle (orange) represent the locations of the equilibrium points (potential minima) of PBP, COCT, IST, and SKEW isomers of the LJ_7 cluster, respectively. By comparing the locations of the respective isomers and the directionality of the twist centrifugal forces in Figs. 5(a) and 5(b), it is expected that the twist centrifugal force $\boldsymbol{f}_{\omega_{12}}$ can drive the structural transitions from oblate isomers such as PBP and IST, whose potential minima are located on the line $a_1 = a_2$ in Fig. 5(a), to prolate isomers such as COCT and SKEW. Similarly, it is also expected that the twist centrifugal force $\boldsymbol{f}_{\omega_{23}}$ can drive the structural transitions from prolate isomers such as COCT and SKEW, whose potential minima are located on/near the line $a_2 = a_3$ in Fig. 5(b), to oblate isomers such as PBP and IST. We will examine these expectations carefully in Sec. III by taking the example of structural transitions between PBP and COCT.

The shear centrifugal forces, the terms proportional to γ_{ik}^2 in Eqs. (22)–(24), have the effects of inflating the mass distributions of the system along the respective principal axes because all these terms always act positively on the respective gyration radii to inflate the overall mass distribution of the system. Roles of these shear centrifugal forces are also of interest in the onset of structural transitions as well as dissociations (evaporations) of clusters.[72]

III. DRIVING MECHANISMS FOR OBLATE-PROLATE TRANSITIONS

In this section, we investigate the driving mechanisms for structural transitions of the LJ_7 cluster between oblate and prolate isomers. We specifically focus on the structural transitions between PBP and COCT as a typical and fundamental example of the structural transitions between oblate and prolate isomers.

A. Gyration radii as collective variables

Figure 6(a) shows a typical time evolution of the three gyration radii, a_1 (solid, red), a_2 (broken, green), and a_3 (dashed-dotted, blue), at total energy $E = -13.5\varepsilon$, where the cluster changes its structure from PBP to COCT. As is evident, the values of a_1 and a_2 are close to each other and apart from the value of a_3 when the system is in the PBP isomer reflecting

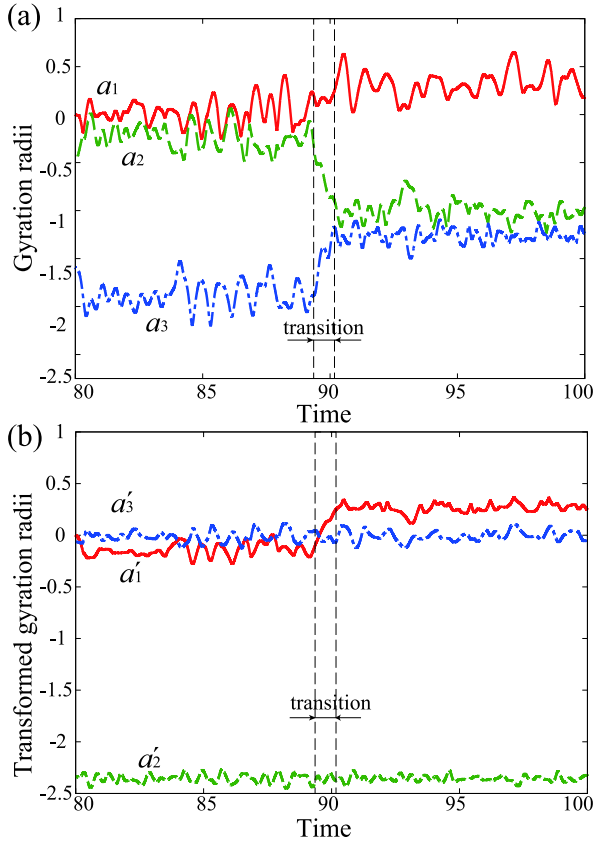

FIG. 6. (a) Typical time evolution of collective variables, the three gyration radii a_1 (solid, red), a_2 (broken, green), and a_3 (dashed-dotted, blue), at total energy $E = -13.5\varepsilon$, where the cluster changes its structure from PBP to COCT. (b) Time evolution of the transformed gyration radii a'_1 (solid, red), a'_2 (broken, green), and a'_3 (dashed-dotted, blue) for the same trajectory as in (a). The vertical dashed lines in the figure represent the time interval where the system is in the transition region defined by Eq. (32).

the oblate mass distribution. When the system is in the COCT isomer, on the other hand, the values of a_2 and a_3 are close to each other and apart from the value of a_1, reflecting the prolate mass distribution. Fig. 6(a) indicates that the three gyration radii are good collective variables to characterize the structural transitions of the cluster.

Since the space of the three gyration radii is Euclidean, it is even more convenient to introduce an orthogonal transformation among the three gyration radii to construct a single reaction coordinate. For this sake, we first introduce a unit vector $\boldsymbol{g}_1$, which is oriented to the direction of the vector linking the averaged position of PBP and that of COCT in the three-dimensional space of gyration radii. For the trajectories of $E = -13.5\varepsilon$, we obtained $\boldsymbol{g}_1 = (0.276, -0.737, 0.616)^T$. This vector characterizes the direction in which the system changes mass distribution most significantly in the three-dimensional space of gyration radii in the structural transitions between PBP and COCT. We then introduce a second unit vector $\boldsymbol{g}_2 = (-0.703, -0.592, -0.394)^T$ which is defined to be perpendicular to $\boldsymbol{g}_1$ and directed to the origin of the space of gyration radii. The third unit vector is defined as $\boldsymbol{g}_3 = \boldsymbol{g}_1 \times \boldsymbol{g}_2 = (0.655, -0.325, -0.682)^T$. Thus, by defining a 3×3 orthogonal matrix $\mathsf{G} = (\boldsymbol{g}_1, \boldsymbol{g}_2, \boldsymbol{g}_3)$, the coordinate transformation $\boldsymbol{a}' = \mathsf{G}^T \boldsymbol{a}$ transforms the original gyration radii $\boldsymbol{a} = (a_1, a_2, a_3)^T$ into the new gyration radii $\boldsymbol{a}' = (a_1', a_2', a_3')^T$. Here, we expect that a_1' changes largely upon structural transitions between PBP and COCT, while a_2' and a_3' do not change significantly. Fig. 6(b) shows the time evolutions of a_1' (solid, red), a_2' (broken, green), and a_3' (dashed-dotted, blue) for the same trajectory as Fig. 6(a). Fig. 6(b) confirms that only a_1' changes largely upon structural transitions between PBP and COCT, while a_2' and a_3' do not change significantly. Thus, the new variable a_1' is a useful variable to signify the structural transitions between PBP and COCT. In this sense, a_1' can be regarded as a reaction coordinate for the structural transitions between PBP and COCT.

For the convenience of the following analysis, we define the *transition region* for the structural transitions between PBP and COCT as the region where the variable a_1' is in the range,

$$-0.1 \le a_1' \le 0.25, \tag{32}$$

which is schematically shown in Figs. 6(a) and 6(b) with dotted vertical lines.

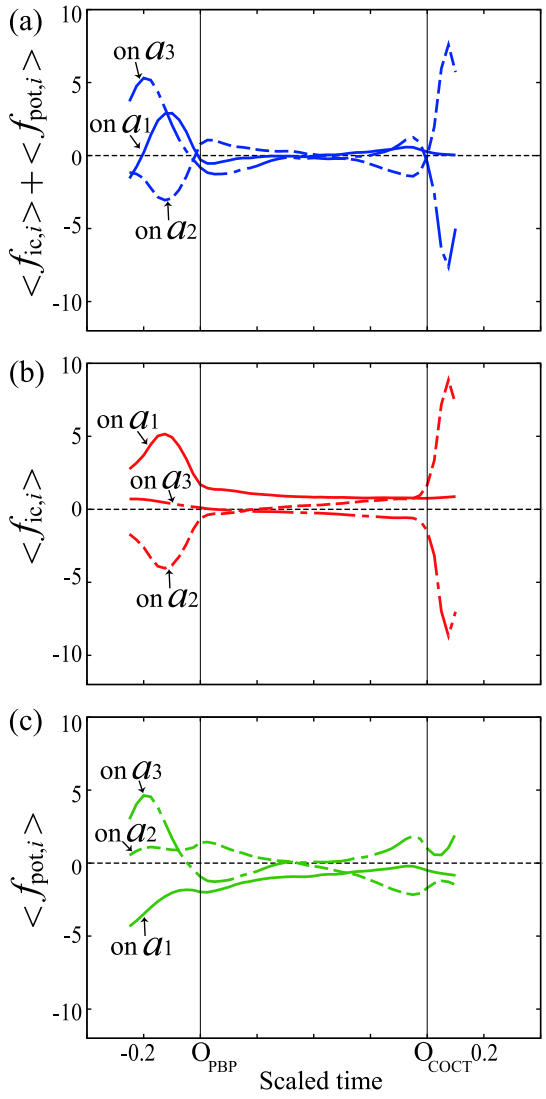

FIG. 7. Averaged time evolutions of the driving forces for structural transitions between PBP to COCT. Panels (a)-(c) show the scaled time evolutions of (a) averaged total force, $\langle f_{\mathrm{ic},i} \rangle + \langle f_{\mathrm{pot},i} \rangle$ ($i = 1, 2, 3$), (b) averaged internal centrifugal force, $\langle f_{\mathrm{ic},i} \rangle$ ($i = 1, 2, 3$), and (c) averaged potential force, $\langle f_{\mathrm{pot},i} \rangle$ ($i = 1, 2, 3$), acting on the three gyration radii, a_1, a_2, and a_3, in the course of structural transitions from PBP to COCT. In (a)-(c), solid curves represent the respective forces acting on a_1, broken curves represent the respective forces acting on a_2, and dashed-dotted curves represent the respective forces acting on a_3. See Eqs. (22)–(26) for the definitions of $f_{\mathrm{ic},i}$ and $f_{\mathrm{pot},i}$.

B. Driving forces for structural transitions

For the purpose of exploring the driving mechanisms for structural transitions, we first study the time evolutions of the forces acting on the three gyration radii, a_1, a_2, and a_3, which serve as the collective variables for structural transitions as we have seen in Fig. 6. According to Fig. 6(a), increase of a_1, decrease of a_2, and increase of a_3 are essential for the structural transitions from PBP to COCT. Therefore, we expect that driving forces should act on a_1 in the positive direction, on a_2 in the negative direction, and on a_3 in the positive direction right before the structural transitions from PBP to COCT. In order to confirm these expectations, Fig. 7 shows averaged and scaled time evolutions of the forces acting on the three gyration radii right before, during, and after structural transitions from PBP to COCT. The horizontal axes of Figs. 7(a)–7(c) represent a scaled time and the vertical axes represent the (a) averaged total force, $\langle f_{\mathrm{ic},i} \rangle + \langle f_{\mathrm{pot},i} \rangle$ ($i = 1, 2, 3$), (b) averaged internal centrifugal force, $\langle f_{\mathrm{ic},i} \rangle$ ($i = 1, 2, 3$), and (c) averaged potential force, $\langle f_{\mathrm{pot},i} \rangle$ ($i = 1, 2, 3$), acting on the three gyration radii. Here, the brackets $\langle \cdot \rangle$ denote an ensemble average over reactive trajectories from PBP to COCT. (See Eqs. (22)–(26) for the definitions of $f_{\mathrm{ic},i}$ and $f_{\mathrm{pot},i}$.) The curves in Fig. 7(a) are essentially the superpositions of those in Figs. 7(b) and 7(c) for the respective components. In Figs. 7(a)–7(c), solid curves represent the respective forces acting on a_1, broken curves represent the respective forces acting on a_2, and dashed-dotted curves represent the respective forces acting on a_3.

The averaging procedure for Figs. 7(a)–7(c) is as follows. We first collect an ensemble of 6189 reactive trajectories from

PBP to COCT at total energy $E = -13.5\varepsilon$ by using the method of Eq. (11). For each of these reactive trajectories, we set the time origin on the PBP side, O_{PBP}, as the last moment at which the trajectory crosses $a_1' = -0.1$ from below before the trajectory moves into the COCT isomer (see Fig. 6(b)). Starting from this time origin, the ensemble of trajectories is averaged at each instant backward in time until $t = -0.25$ (in dimensionless unit). This procedure gives the portions of the curves in the range $-0.25 \le t \le O_{PBP}$ in Figs. 7(a)–7(c). In the same manner, we set another time origin on the COCT side, O_{COCT}, as the first moment at which the trajectory crosses the line $a_1' = 0.25$ from below after the trajectory comes into the COCT isomer. Starting from this time origin, the ensemble of trajectories is averaged at each instant forward in time until $t = 0.1$ (in dimensionless unit). This procedure gives the portions of the curves in the range $O_{COCT} \le t \le 0.1$ in Figs. 7(a)–7(c). As for the curves in the range $O_{PBP} \le t \le O_{COCT}$ in Figs. 7(a)–7(c), we divided the portion of each reactive trajectory lying in the transition region into 32 time windows and averaged in the respective time windows over the ensemble of reactive trajectories. Therefore, the length of the time span $O_{PBP} \le t \le O_{COCT}$ in Figs. 7(a)–7(c) is arbitrary and not to scale exactly.

As we see from Fig. 7(a), a_1 is subject to the strong total force in the positive direction, and a_2 is subject to the strong total force in the negative direction, and a_3 is subject to the strong total force in the positive direction right before the structural transitions from PBP to COCT, i.e., right before O_{PBP}. This result confirms our expectations that we made at the beginning of this subsection. Moreover, from Figs. 7(b) and 7(c), it becomes clear that both the positive total force on a_1 and the negative total force on a_2 right before the structural transitions from PBP to COCT are due to the internal centrifugal force. This indicates that the internal centrifugal force plays a crucial role for the onset of structural transitions from PBP to COCT by breaking the symmetry (equality) between a_1 and a_2. The positive total force on a_3 right before the structural transitions from PBP to COCT is mainly due to the potential force (see Fig. 7(c)).

In order to discuss the reverse reaction, i.e., the structural transition from COCT to PBP, it is sufficient to look at Fig. 7 in the reversed direction, from right to left, by virtue of the time-reversal symmetry of the Hamiltonian dynamics. For the structural transitions from COCT to PBP, decrease of a_1, increase of a_2, and decrease of a_3 are essential as we see from Fig. 6(a). Therefore, we expect that the total force should be acting on a_1 in the negative direction, on a_2 in the positive direction, and on a_3 in the negative direction right before the structural transitions from COCT to PBP. The results of Fig. 7(a) show that this is almost the case. That is, a_2 is subject to the strong total force in the positive direction, and a_3 is subject to the strong total force in the negative direction right before the structural transitions from COCT to PBP. The total force on a_1 is almost zero right before the structural transitions from COCT to PBP. This is reasonable because the change in a_1 is small compared to the changes in a_2 and a_3 for the structural transitions between COCT and PBP. From Figs. 7(b) and 7(c), it becomes clear that both the positive total force on a_2 and the negative total force on a_3 right before the structural transitions from COCT to PBP are mostly due to the internal centrifugal force. Since breaking the symmetry between a_2 and a_3 is crucial for the onset of structural transitions from the prolate isomer (COCT) to the oblate isomer (PBP), we see that the internal centrifugal force is the primary driving force for the structural transitions COCT to PBP.

C. Characterization of the driving forces in the space of gyration radii

We characterize here the driving forces for structural transitions revealed in Subsection III B in the space of gyration radii, a_1, a_2, and a_3, using the a_1-a_2 and a_3-a_2 planes, introduced in Fig. 2. We again note that these planes are Euclidean as explained in Sec. II D so that investigations on the directionality of force fields on these planes as in Fig. 5 are meaningful.

Figure 8 shows averaged force fields on the planes of gyration radii for three different situations in the dynamics of the cluster. Panels (a)-(f) show the projections of the average force fields of the ((a) and (d)) total force, $\langle \boldsymbol{f}_{ic} \rangle + \langle \boldsymbol{f}_{pot} \rangle$, ((b) and (e)) internal centrifugal force, $\langle \boldsymbol{f}_{ic} \rangle$, and ((c) and (f)) potential force, $\langle \boldsymbol{f}_{pot} \rangle$, where the average $\langle \cdot \rangle$ is taken over an ensemble of trajectories that are in the potential well of PBP or that of COCT. (See Eqs. (27) and (28) for the definitions of $\boldsymbol{f}_{ic}$ and $\boldsymbol{f}_{pot}$.) This average does not include the portions of reactive trajectories right before structural transitions and just inside the transition region defined in Eq. (32). Therefore, all the force fields in panels (a)-(f) are regarded as "*equilibrium*" force fields in the PBP and COCT isomers since these force fields are averaged over many trajectories that correspond to relatively stable vibrations in these two isomers, and are not directly associated with structural transitions. As shown, panels (a)-(c) are the projections on the a_1-a_2 plane and panels (d)-(f) are the projections on the a_3-a_2 plane. The internal centrifugal force in Fig. 8(b) possesses the clear directionality to increase a_1 and decrease a_2 near the line, $a_1 = a_2$. The internal centrifugal force in Fig. 8(e) also possesses the clear directionality to increase a_2 and decrease a_3 near the line, $a_2 = a_3$. These tendencies are due to the symmetry breaking effect of the twist centrifugal force that we have seen in Fig. 5. The averaged field of the potential force in Figs. 8(c) and 8(f) shows the directionality to the two minima of the potential energy corresponding to PBP and COCT.

Panels (a′)-(f′) in Fig. 8 show the projections of the averaged force fields of the ((a′) and (d′)) total force, $\langle \boldsymbol{f}_{ic} \rangle + \langle \boldsymbol{f}_{pot} \rangle$, ((b′) and (e′)) internal centrifugal force, $\langle \boldsymbol{f}_{ic} \rangle$, and ((c′) and (f′)) potential force, $\langle \boldsymbol{f}_{pot} \rangle$, *right before the cluster undergoes structural transitions from PBP to COCT*. Panels (a′)-(c′) are the projections on the a_1-a_2 plane and panels (d′)-(f′) are the projections on the a_3-a_2 plane. In these panels (a′)-(f′), the force fields exist only in the region of the PBP isomer because the average is taken over an ensemble of trajectories right before undergoing transitions from PBP to COCT. It is clearly seen that the fields of the internal centrifugal force in panels (b′) and (e′) are much stronger and possess the much clearer directionality from PBP to COCT than those in panels (b) and (e) in the region of the PBP isomer. It is also important to note that the internal centrifugal force in Fig. 8(b′) has the clear directionality to break the equality (symmetry) between a_1 and a_2, which is essential in triggering the transitions from

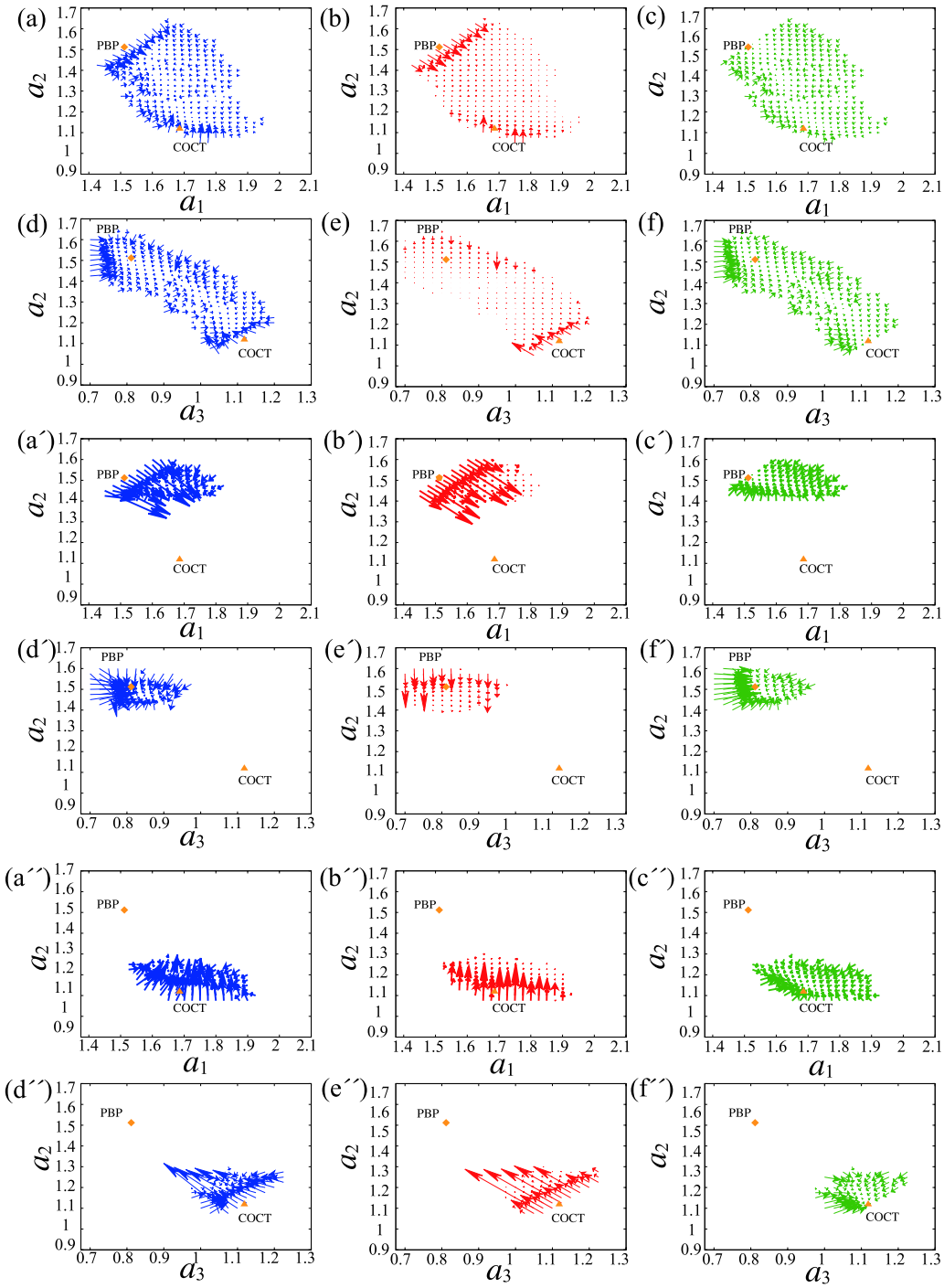

FIG. 8. Comparison of averaged force fields on the planes of gyration radii in "equilibrium" and at the onset of structural transitions between PBP and COCT. Panels (a)-(c), (a′)-(c′), (a″)-(c″) are the projections on the a_1-a_2 plane and panels (d)-(f), (d′)-(f′), (d″)-(f″) are the projections on the a_3-a_2 plane. Panels (a)-(f) show the "*equilibrium*" force fields of the ((a) and (d)) total force, $\langle \boldsymbol{f}_{\rm ic} \rangle + \langle \boldsymbol{f}_{\rm pot} \rangle$, ((b) and (e)) internal centrifugal force, $\langle \boldsymbol{f}_{\rm ic} \rangle$, and ((c) and (f)) potential force, $\langle \boldsymbol{f}_{\rm pot} \rangle$. See the main text for the definition of "equilibrium." (See Eqs. (27) and (28) for the definitions of $\boldsymbol{f}_{\rm ic}$ and $\boldsymbol{f}_{\rm pot}$.) Panels (a′)-(f′) show the averaged force fields of the ((a′) and (d′)) total force, $\langle \boldsymbol{f}_{\rm ic} \rangle + \langle \boldsymbol{f}_{\rm pot} \rangle$, ((b′) and (e′)) internal centrifugal force, $\langle \boldsymbol{f}_{\rm ic} \rangle$, and ((c′) and (f′)) potential force, $\langle \boldsymbol{f}_{\rm pot} \rangle$, *right before the cluster undergoes structural transitions from PBP to COCT*. Panels (a″)-(f″) show the averaged force fields of the ((a″) and (d″)) total force, $\langle \boldsymbol{f}_{\rm ic} \rangle + \langle \boldsymbol{f}_{\rm pot} \rangle$, ((b″) and (e″)) internal centrifugal force, $\langle \boldsymbol{f}_{\rm ic} \rangle$, and ((c″) and (f″)) potential force, $\langle \boldsymbol{f}_{\rm pot} \rangle$, *right before the cluster undergoes structural transitions from COCT to PBP*. In each panel, locations of the local minima of potential energy are indicated with a diamond for PBP and with a triangle for COCT.

the oblate isomer like PBP. Since the components of the twist centrifugal force that are proportional to ω_{12}^2 have this directionality of breaking the equality (symmetry) between a_1 and a_2, we expect that activation of the ω_{12} mode is crucial for the transition from PBP to COCT. We will confirm this point in Sec. IV. These results can be a clear evidence for the fact that the internal centrifugal force drives the structural transitions from PBP to COCT at the onset of transition. Averaged fields of potential force in Figs. 8(c′) and 8(f′), on the other hand, are not very different from those in Fig. 8(c) and 8(f) in the region of the PBP isomer. That is, in both Figs. 8(c) and 8(f) and Figs. 8(c′) and 8(f′), the potential force fields are directed towards the

minimum of the PBP isomer in its vicinity. It is noticeable that the potential force field in Fig. 8(f′) possesses a stronger and clearer directionality to increase a_3 than in Fig. 8(f). This is consistent with the fact that the increase of a_3 in the transitions from PBP to COCT is mainly driven by the potential force as we have seen in Fig. 7.

We next investigate the driving forces for the reverse reaction from COCT to PBP in the same manner. Panels (a″)-(f″) in Fig. 8 show the projections of the averaged force fields of the ((a″) and (d″)) total force, $\langle \boldsymbol{f}_{\rm ic} \rangle + \langle \boldsymbol{f}_{\rm pot} \rangle$, ((b″) and (e″)) internal centrifugal force, $\langle \boldsymbol{f}_{\rm ic} \rangle$, and ((c″) and (f″)) potential force, $\langle \boldsymbol{f}_{\rm pot} \rangle$, *right before the cluster undergoes structural transitions from COCT to PBP*. Panels (a″)-(c″) are the projections on the a_1-a_2 plane and panels (d″)-(f″) are the projections on the a_3-a_2 plane. In these panels (a″)-(f″), the force fields exist only in the region of the COCT isomer because the average is taken over an ensemble of trajectories right before undergoing the transitions from COCT to PBP. It is clearly seen that the fields of the internal centrifugal force in panels (b″) and (e″) are much stronger and possess the much clearer directionality from COCT to PBP than those in panels (b) and (e) in the region of the COCT isomer. It is also important to note that the internal centrifugal force in Fig. 8(e″) has the clear directionality to break the equality (symmetry) between a_2 and a_3, which is essential in triggering the transitions from the prolate isomer like COCT. Since the components of the twist centrifugal force that are proportional to ω_{23}^2 have this directionality of breaking the equality (symmetry) between a_2 and a_3, we expect that activation of the ω_{23} mode is crucial for the transition from COCT to PBP. We will confirm this point in Sec. IV. These results can be a clear evidence for the fact that the internal centrifugal force drives the structural transitions from COCT to PBP at the onset of transition. Averaged fields of potential force in Figs. 8(c″) and 8(f″), on the other hand, are not very different from those in Figs. 8(c) and 8(f) in the region of the COCT isomer. That is, in both Figs. 8(c) and 8(f) and Figs. 8(c″) and 8(f″), the potential force fields are directed towards the minimum of the COCT isomer in its vicinity.

D. Intramolecular energy transfer before, during, and after structural transitions

We investigate here the mechanisms for structural transitions between the oblate and prolate isomers from the viewpoint of energy transfer among the hyperspherical modes. Results presented here can be the basis for the selective activations of hyperspherical modes in Sec. IV. Analysis of this subsection stems from the compact expression of internal kinetic energy in the hyperspherical coordinates in Eq. (12), where the first three terms proportional to $\dot{a}_i^2$ $(i = 1,2,3)$ are kinetic energies for the gyration-radius modes, the next three terms proportional to ω_{ij}^2 $(ij = 12,23,31)$ are kinetic energies for the twisting modes, and the terms proportional to γ_{ik}^2 $(i = 1,2,3,\ k = 4,5,6)$ are kinetic energies for the shearing modes.

Fig. 9 shows the averaged and scaled time evolutions of the partitioning of kinetic energy over the hyperspherical modes before, during, and after structural transitions. Fig. 9(a) is for the structural transitions from PBP to COCT, while Fig. 9(b) is for the structural transitions from COCT to PBP. In both Figs. 9(a) and 9(b), denseness of the plot (color) represents the relative amount of kinetic energy in the respective hyperspherical modes (arranged vertically) and in the respective time windows (arranged horizontally) as scaled by the scale bar on the right. In every time window, the amount of kinetic energy in each mode is scaled with respect to the total kinetic energy and is averaged over an ensemble of reactive trajectories. As for the 9 kinetic energies for the shearing modes, γ_{ik} $(i = 1,2,3,\ k = 4,5,6)$, we average over the second subscripts k and reduced to the three kinetic energies, which are shown in the bottom three rows labeled as γ_i $(i = 1,2,3)$ in Figs. 9(a) and 9(b). This is because there is an arbitrariness in the definitions of the second subscripts k for the shearing modes, γ_{ik} $(i = 1,2,3,\ k = 4,5,6)$, as noted in Ref. 71.

The procedures of averaging and scaling in Figs. 9(a) (and 9(b)) are similar to those for Fig. 7. That is, we first collect an ensemble of 6189 reactive trajectories from PBP to COCT at total energy $E = -13.5\varepsilon$. For each of these reactive

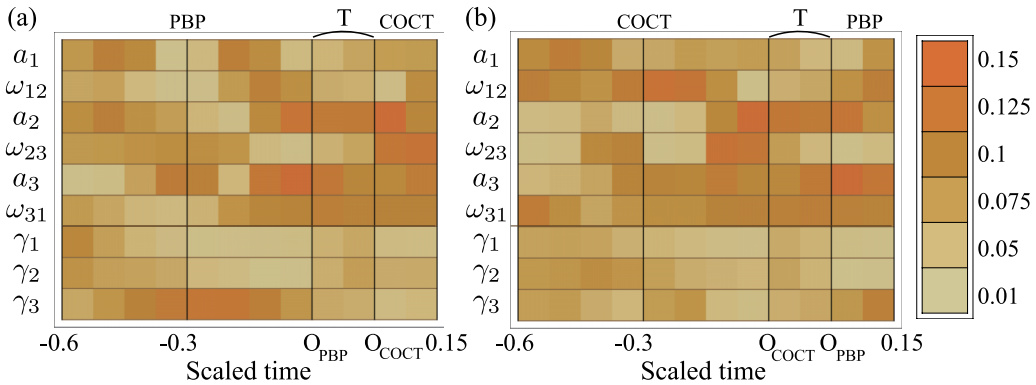

FIG. 9. Identification of active modes (driving modes) at the onset of structural transitions. Panels (a) and (b) show averaged and scaled time evolutions of the partitioning of kinetic energy over the hyperspherical modes before, during, and after structural transitions at total energy $E = -13.5\varepsilon$. (a) is for the transitions from PBP to COCT. (b) is for the transitions from COCT to PBP. Denseness of the plot (color) represents the relative amount of kinetic energy in the respective hyperspherical modes (arranged vertically) and in the respective time windows (arranged horizontally) as shown by the scale bar on the right. Notice that, in both (a) and (b), a_2-, a_3-, and ω_{31}-modes are active when the cluster is in the transition region, which is indicated by the label "T," undergoing structural transitions. Notice also that ω_{12}- and γ_3-modes are active right before the structural transitions from PBP to COCT in (a), while ω_{23}-mode is active right before the structural transitions from COCT to PBP in (b).

trajectories, we set the time origin on the PBP side O_{PBP} at the last moment at which the trajectory crosses $a_1' = -0.1$ from below before the trajectory moves into the COCT isomer (see Eq. (32) and Fig. 6(b)). Thus, we assign the time origin O_{PBP} to all the reactive trajectories. Starting from this time origin, energy partitioning is averaged over the ensemble of reactive trajectories backward in time in each time window until $t = -0.6$. Each time window has the time span of 0.075 (in dimensionless unit). This procedure gives the portion of the diagram of Fig. 9(a) in the range $-0.6 \le t \le O_{PBP}$, which consists of $0.6/0.075 = 8$ time windows. In the same manner, we set another time origin on the COCT side O_{COCT} for each reactive trajectory at the first moment at which the trajectory crosses the line $a_1' = 0.25$ from below after the trajectory comes into the COCT isomer (see Eq. (32) and Fig. 6(b)). Starting from this time origin, energy partitioning is averaged over the ensemble of trajectories forward in time in each time window until $t = 0.15$. Again each time window has the time span of 0.075 (in dimensionless unit). This procedure gives the portion of the diagram of Fig. 9(a) in the range $O_{PBP} \le t \le 0.15$. As for the energy partitioning in the time interval between O_{PBP} and O_{COCT}, which is labeled as "T" (meaning the transition region defined by Eq. (32)) in Fig. 9(a), we divided the portion of each reactive trajectory lying in the transition region into 2 time windows and averaged over the ensemble of reactive trajectories in each time window. Therefore, the length of the time span between O_{PBP} and O_{COCT} in Fig. 9(a) is rather arbitrary and not to scale. The procedures of averaging and scaling in Fig. 9(b) are essentially the same as those in Fig. 9(a) except that the roles of PBP and COCT are switched.

From Figs. 9(a) and 9(b), we first see that both a_2 and a_3 are active, possessing a large amount of kinetic energy, when the cluster is in the transition region undergoing structural transitions between PBP and COCT in either direction (see the time intervals labeled as "T" in Figs. 9(a) and 9(b)). This is consistent with the fact that both a_2 and a_3 change significantly (see Fig. 6(a)) after driven by the strong forces (see Fig. 7(a)) in the structural transitions between PBP and COCT in either direction. It is also noticeable from Figs. 9(a) and 9(b) that the ω_{31}-mode possesses a large amount of kinetic energy when the cluster is in the transition region undergoing structural transitions between PBP and COCT in either direction. The reason for this activeness of the ω_{31}-mode will be discussed at the end of this section in terms of the movement of principal axes during the structural transitions.

We next look into the energy partitioning right before the structural transitions. It can be seen from Fig. 9(a) that ω_{12}-mode is *active* and ω_{23}-mode is *inactive* and γ_3-mode is *active* right before the structural transitions from PBP to COCT. The reason for the activeness of ω_{12}-mode right before the structural transitions is that ω_{12}-mode is the source of the strong twist centrifugal force $\boldsymbol{f}_{\omega_{12}}$ (see Eq. (29)), which has the effect of breaking the symmetry between a_1 and a_2 of the oblate mass distribution of PBP as we have discussed in Fig. 5. In other words, the activeness of ω_{12}-mode is the reflection of the fact that ω_{12}-mode drives the structural transitions from PBP by inducing the strong internal centrifugal force as we have seen in Fig. 7(b) and Fig. 8(b′). The inactiveness of ω_{23}-mode right before structural transitions from PBP to COCT originates from the fact that ω_{23}-mode generally induces the strong internal centrifugal force $\boldsymbol{f}_{\omega_{23}}$ (see Eq. (30)), which has the effect of increasing a_2 and decreasing a_3 and blocks the structural transitions from PBP to COCT. Therefore, the ω_{23}-mode needs to be inactive right before structural transitions from PBP to COCT. The activeness of the γ_3-mode right before structural transitions from PBP to COCT originates from the fact that the γ_3-mode has the general effect of inducing the shear centrifugal force, the term proportional to γ_{3k}^2 in Eq. (24), which has the effect of increasing a_3. Since the increase of a_3 is crucial for the structural transitions from PBP to COCT (see Fig. 6(a)), activation of the γ_3-mode promotes transitions from PBP to COCT. We thus see that the energy partitioning right before structural transitions from PBP to COCT in Fig. 9(a) is consistent with the driving mechanisms presented in Subsections III B and III C.

In the same manner, we can check the consistency of the energy partitioning right before structural transitions from COCT to PBP in Fig. 9(b) with the driving mechanism for structural transitions as follows. From Fig. 9(b), we see that ω_{12}-mode is *inactive* and ω_{23}-mode is *active* and γ_3-mode is *inactive* right before the structural transitions from COCT to PBP. This is in clear contrast to the energy partitioning right before the structural transitions from PBP to COCT in Fig. 9(a). The reason for the activeness of ω_{23}-mode right before the structural transitions from COCT to PBP is that ω_{23}-mode is the source of the strong twist centrifugal force $\boldsymbol{f}_{\omega_{23}}$ (see Eq. (30)), which has the effect of breaking the symmetry between a_2 and a_3 of the prolate mass distribution of COCT. In other words, the active ω_{23}-mode is the reflection of the fact that ω_{23}-mode drives the structural transitions from COCT by inducing the strong internal centrifugal force as we have seen in Fig. 7(b) and Fig. 8(b″). The inactiveness of ω_{12}-mode right before structural transitions from COCT to PBP originates from the fact that ω_{12}-mode generally induces the strong internal centrifugal force $\boldsymbol{f}_{\omega_{12}}$ (see Eq. (29)), which has the effect of increasing a_1 and decreasing a_2 and blocks the structural transitions from COCT to PBP. Therefore, the ω_{12}-mode needs to be inactive right before structural transitions from COCT to PBP. The inactiveness of the γ_3-mode right before the structural transitions from COCT to PBP originates from the fact that the γ_3-mode has the general effect of inducing the shear centrifugal force, the term proportional to γ_{3k}^2 in Eq. (24), which has the effect of increasing a_3. Since the increase of a_3 counteracts the directionality of structural transitions from COCT to PBP (see Fig. 6(a)), the γ_3-mode needs to be inactive right before the structural transitions from COCT to PBP. We, thus, see that the energy partitioning right before structural transitions from COCT to PBP in Fig. 9(b) is consistent with the driving mechanisms presented in Subsections III B and III C.

Finally, we discuss the reason for the activeness of the ω_{31}-mode throughout the whole processes of structural transitions between PBP and COCT in either direction observed in Figs. 9(a) and 9(b). Fig. 10 shows a typical movement of the three principal axes before, during, and after a structural transition from PBP to COCT. The visualization scheme of Fig. 10 is the same as Fig. 3. When the system is in the PBP isomer, an oblate isomer, the first and second principal

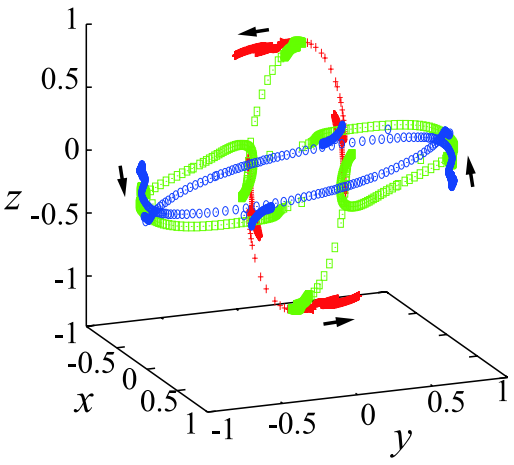

FIG. 10. Typical movements of the three principal axes in the course of a structural transition from PBP to COCT. Visualization scheme is the same as Fig. 3. Crosses (red), squares (green), and circles (blue) represent the movements of the "heads" of the first, second, and third principal axes, respectively. The four arrows represent the coupling and corotation of the first and third principal axes right in the course of structural transition from PBP to COCT.

axes couple together and corotate forming a "ring," while the third principal axis is almost fixed in the three dimensional space as we have seen in Fig. 3(a). When the system is in the COCT isomer, a prolate isomer, the second and third principal axes couple together and corotate forming a "ring," while the first principal axis is almost fixed in the three dimensional space as we have seen in Fig. 3(b). Therefore, the process of structural transition corresponds to the movements of the principal axes interconnecting these two typical movement patterns. From Fig. 10, it is clearly seen that the first and third principal axes couple together and corotate as indicated by the four arrows when the system switches between the two typical movement patterns of PBP and COCT. This fact indicates that the coupling between the first and third principal axes is also a necessary requirement for the structural transitions between PBP and COCT in addition to the significant change in the gyration radii. According to Eq. (18), the coupling between the first and third principal axes, which is characterized by Ω_{31}, is directly driven by the twisting motion characterized by ω_{31}. Thus, the reason for the activeness of ω_{31}-mode in the course of structural transitions between PBP and COCT stems from the fact that the first and third principal axes need to couple and corotate in the course of the structural transition.

IV. INDUCING STRUCTURAL TRANSITIONS VIA SELECTIVE ACTIVATIONS OF HYPERSPHERICAL MODES

In Sec. III, we have evidenced that the structural transitions of the LJ_7 cluster are driven by the forces acting on the gyration radii and the movements of principal axes. Moreover, the forces acting on gyration radii and the movements of principal axes are mediated by the activities, i.e., partitioning of kinetic energy, of the twisting modes and the shearing modes. Based on this knowledge, this section explores the possibility of inducing structural transitions of the cluster by selectively activating specific hyperspherical modes.

A. Inducing structural transitions from PBP (oblate) to COCT (prolate)

We first investigate the transitions from the PBP isomer (oblate) to the COCT isomer (prolate). As noticed from Figs. 6(a) and 8(b′), breaking the symmetry (equality) between a_1 and a_2 is essential for the initiation of the transition from PBP to COCT. Since the twist centrifugal force proportional to ω_{12}^2, i.e., $\boldsymbol{f}_{\omega_{12}}$ defined in Eq. (29), has the directionality of breaking this symmetry (equality) between a_1 and a_2 as we noted in Fig. 5(a), we expect that activation of the ω_{12}-mode is crucial for the transition from PBP to COCT. Indeed, we have evidenced in Fig. 9(a) that the ω_{12}-mode tends to be active at the onset of transitions from PBP to COCT. In addition, since the increase of a_3 is also important for this transition from PBP to COCT as noted in Fig. 6(a), activation of a_3 would also be important for the structural transition from PBP to COCT.

Keeping these initial thoughts in mind, we carry out the following numerical experiments. We first set an initial configuration of the cluster randomly near the equilibrium point of the PBP isomer. We then activate two of the hyperspherical modes simultaneously by assigning initial velocities to the respective atoms so that these two modes possess the same amount of kinetic energy. These two modes are chosen among the three gyration-radius modes and the three twisting modes. Therefore, we examine ${}_6C_2 = 15$ combinations of the initially activated modes in total. We scale the magnitudes of initial velocities of atoms so that the total energy of the cluster is always $E = -13.5\varepsilon$. We then measure the dwell time (waiting time) until the cluster undergoes the transition to the COCT isomer. We discard the trajectories that undergo transitions to the IST or SKEW isomer for the purposes of focusing on the transitions from PBP to COCT only. In addition, we discard the trajectories that do not undergo any transition within 50 dimensionless time for simplicity. We repeat this procedure for 1000 random initial configurations around the equilibrium point of the PBP isomer, and obtain a distribution of the dwell time.

It should be noted that we do not activate any of the nine shearing modes initially in the present numerical experiment for simplicity. This is also because the gyration-radius modes and the twisting modes are expected to play more dominant roles than the shearing modes in the onset of structural transitions that accompany significant changes in mass distributions of the system according to the results in Sec. III. It should also be noted that when we activate a gyration-radius mode, we choose the direction of the initial velocities of atoms so that the velocity of the gyration radius possesses the directionality that is "favorable" for the structural transition from PBP to COCT. For example, when we activate the a_1-mode, we set the initial velocities of atoms so that $\dot{a}_1$ be positive, since a_1 generally need to increase in order for the system to change from PBP to COCT (see Fig. 6(a)). Similarly, when we activate the a_2-mode, we set the initial velocities of atoms so that $\dot{a}_2$ be negative, since a_2 generally need to decrease in order for the system to change from PBP to COCT. When we activate the a_3-mode, we set the initial velocities of atoms so that $\dot{a}_3$ be positive, since a_3 generally need to increase in order for the system to change from PBP to COCT.

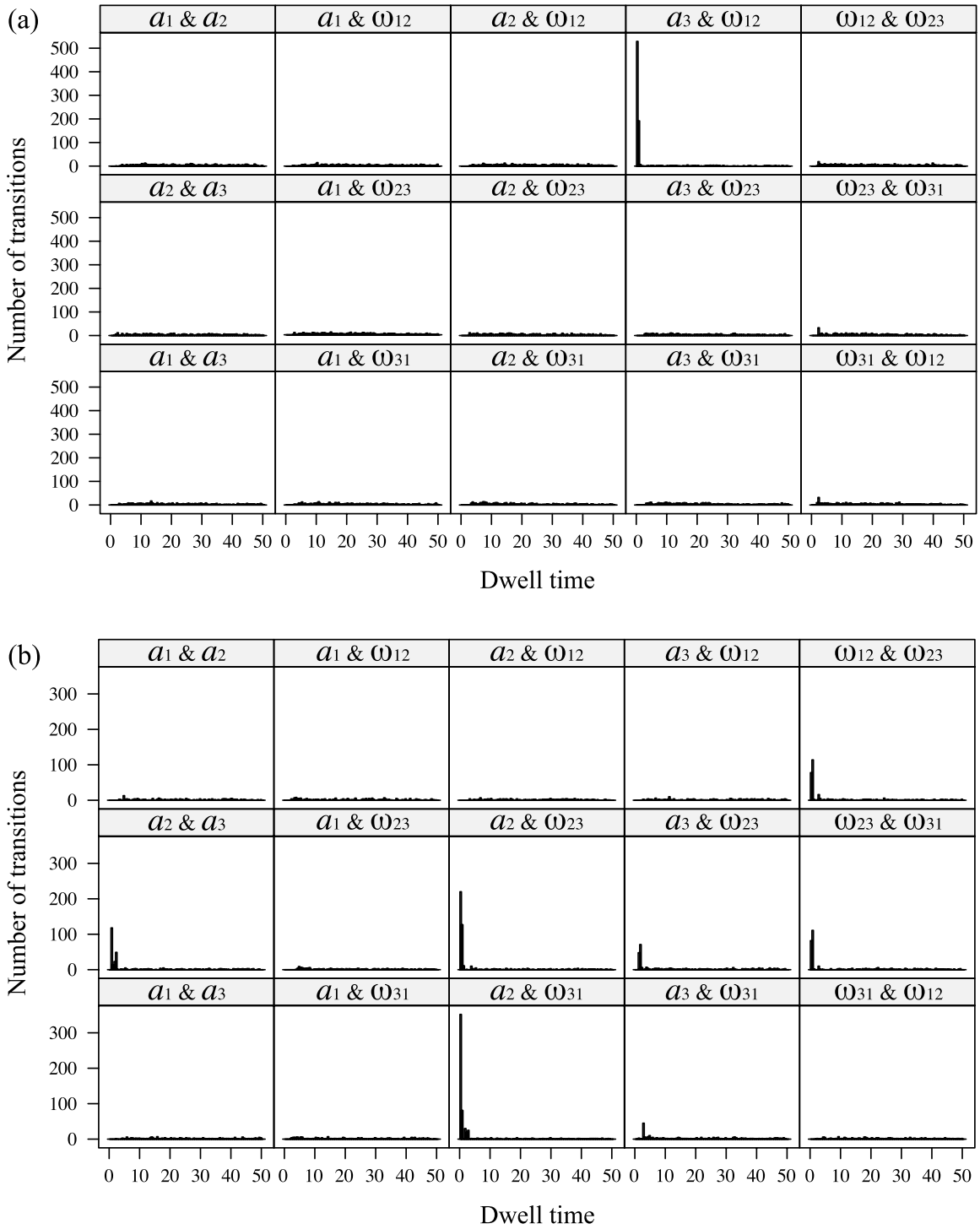

FIG. 11. (a) Histograms of dwell time for the transitions from PBP to COCT after activating the 15 combinations of two hyperspherical modes in PBP at $E = -13.5\varepsilon$. (b) Histograms of dwell time for the transitions from COCT to PBP after activating the 15 combinations of two hyperspherical modes in COCT at $E = -14.5\varepsilon$. For each panel, two initially activated modes are indicated above. In each of (a) and (b), all panels have the same plotting range. Notice from (a) that only the simultaneous activation of a_3- and ω_{12}-modes induces a quite large number of immediate structural transitions from PBP to COCT. Notice from (b) that simultaneous activations of the following combinations of modes induce markedly large number of immediate transitions from COCT to PBP: (a_2, ω_{31}), (a_2, ω_{23}), $(\omega_{12}, \omega_{23})$, (a_2, a_3), $(\omega_{23}, \omega_{31})$, (a_3, ω_{23}).

Figure 11(a) shows the histograms of dwell time for the transitions from PBP to COCT after activating the 15 combinations of hyperspherical modes at $E = -13.5\varepsilon$. Left half of Table II summarizes the average dwell times in PBP computed from the histograms of Fig. 11(a) in the order of shorter dwell time. As clearly seen from Fig. 11(a), only the simultaneous activation of the a_3- and ω_{12}-modes induces a quite large number of immediate structural transitions (within 3 dimensionless time) from PBP to COCT effectively. This is also seen from the fact that the average dwell time in Table II is markedly short (4.18 dimensionless time) for the simultaneous activation of the a_3- and ω_{12}-modes. Activations of other combinations of

TABLE II. Left half of the table shows the average dwell times for the transitions from PBP to COCT after activating the 15 combinations of two hyperspherical modes at $E = -13.5\varepsilon$. Data are sorted in the order of shorter dwell time. Right half of the table shows the average dwell times for the transitions from COCT to PBP after activating the 15 combinations of two hyperspherical modes at $E = -14.5\varepsilon$. Data are sorted in the order of shorter dwell time.

PBP		COCT	
Modes	Dwell time	Modes	Dwell time
a_3, ω_{12}	4.18	a_2, ω_{31}	5.17
ω_{12}, ω_{31}	20.84	a_2, ω_{23}	6.69
ω_{23}, ω_{31}	21.38	ω_{12}, ω_{23}	10.53
a_2, ω_{31}	21.80	a_2, a_3	11.38
ω_{12}, ω_{23}	22.35	ω_{23}, ω_{31}	11.81
a_3, ω_{31}	22.85	a_3, ω_{23}	15.36
a_2, ω_{23}	22.86	a_3, ω_{31}	19.83
a_1, ω_{23}	23.10	a_1, ω_{12}	22.65
a_3, ω_{23}	23.22	a_1, ω_{23}	22.67
a_1, ω_{31}	23.49	a_1, ω_{31}	22.85
a_1, a_3	23.92	a_1, a_2	24.02
a_2, a_3	24.01	ω_{12}, ω_{31}	24.35
a_2, ω_{12}	24.50	a_2, ω_{12}	24.82
a_1, a_2	24.98	a_1, a_3	25.18
a_1, ω_{12}	25.00	a_3, ω_{12}	25.96

modes do not give very different results in terms of the distributions of dwell time (Fig. 11(a)) as well as the average dwell times (Table II). This result confirms our initial expectations on the importance of activation of a_3- and ω_{12}-modes made at the beginning of this subsection. The effectiveness of activating the ω_{12}-mode stems from the fact that this mode induces the twist centrifugal force $\boldsymbol{f}_{\omega_{12}}$ defined in Eq. (29) that breaks the equality (symmetry) between a_1 and a_2, which is essential for the initiation of structural transitions from an oblate isomer. The effectiveness of activating the a_3-mode stems from the fact that a_3 needs to increase largely for the transitions from PBP to COCT (see Fig. 6(a)).

B. Inducing structural transitions from COCT (prolate) to PBP (oblate)

We next investigate the transitions from the COCT isomer (prolate) to the PBP isomer (oblate). As noticed from Fig. 6(a) and Fig. 8(e″), breaking the symmetry (equality) between a_2 and a_3 is essential for the initiation of the transition from COCT to PBP. Since the twist centrifugal force proportional to ω_{23}^2, i.e., $\boldsymbol{f}_{\omega_{23}}$ defined in Eq. (30), has the directionality of breaking this symmetry (equality) between a_2 and a_3 as noted in Fig. 5(b), we expect that activation of the ω_{23}-mode is crucial for the transition from COCT to PBP. Indeed, we have evidenced in Fig. 9(b) that the ω_{23}-mode tends to be active at the onset of transitions from COCT to PBP.

Fig. 11(b) shows the histograms of dwell time for the transitions from COCT to PBP after activating the 15 combinations of hyperspherical modes. Right half of Table II summarizes the average dwell times in COCT computed from the distributions of Fig. 11(b) in the order of shorter dwell time. The numerical procedure for obtaining Fig. 11(b) is essentially the same as Fig. 11(a) except that the initial configurations of the cluster are randomly set around the equilibrium structure of the COCT isomer and that the total energy is $E = -14.5\varepsilon$. Note that we have lowered the total energy to $E = -14.5\varepsilon$ for the COCT isomer as compared to $E = -13.5\varepsilon$ for the PBP isomer. This is because the transitions from COCT to PBP tend to occur much faster than the transitions from PBP to COCT at the same energy level, and the distinction between the most effective combinations of initially activated modes and others was not very clear at $E = -13.5\varepsilon$. This would be because the potential well of COCT is shallower than PBP, and the COCT is more "fragile" than PBP. Therefore, in order to see the distinction between the effective combinations of initially activated modes and others clearer, we lowered the total energy to $E = -14.5\varepsilon$. In addition, when we activate a gyration-radius mode, we choose the direction of the initial velocities of atoms so that the velocity of the gyration radius possesses the directionality that is "favorable" for the structural transition from COCT to PBP as in Sec. IV A.

According to the results of Fig. 11(b) and Table II, simultaneous activations of the following combinations of modes induce markedly large number of immediate transitions from COCT to PBP: (a_2,ω_{31}), (a_2,ω_{23}), $(\omega_{12},\omega_{23})$, (a_2,a_3), $(\omega_{23},\omega_{31})$, (a_3,ω_{23}). Since the ω_{23}-mode appears frequently in this list, we readily see that activation of the ω_{23}-mode is important for the initiation of the transition from COCT to PBP. This is consistent with our expectation made at the beginning of the present subsection. It is also noticeable that activation of the ω_{31}-mode is effective in inducing transitions from COCT to PBP. Indeed, the most effective combination in inducing transitions from COCT to PBP is (a_2,ω_{31}) according to Table II. The importance of activation of the ω_{31}-mode is understood from the fact that the first and the third principal axes must couple and corotate for the structural transition between COCT and PBP as we have seen in Fig. 10.

V. CONCLUDING REMARKS

We have presented the driving mechanisms for structural transitions of the seven-atom Lennard-Jones cluster (LJ_7) between oblate and prolate isomers in terms of the coarse-grained dynamics of three gyration radii and three principal axes of the system. Dynamics of gyration radii is essentially governed by the potential force and by the dynamical forces called the internal centrifugal forces originating from the twisting and shearing motions of the system. The internal centrifugal force arising from twisting motions has an effect of breaking the symmetry between two gyration radii. As a result, in an oblate isomer of the cluster (PBP), activation of the internal centrifugal force that has the effect of breaking the symmetry between the two largest gyration radii can trigger structural transitions into a prolate isomer (COCT). In a prolate isomer (COCT), on the other hand, activation of the internal centrifugal force that has the effect of breaking the symmetry between the two smallest gyration radii can trigger structural transitions into an oblate isomer (PBP). Activation of the twisting motion (ω_{31}-mode) that switches the movement patterns of three principal axes is also important for the onset of structural transitions between the oblate and prolate isomers. Based on these trigger

mechanisms, we have finally induced structural transitions of the cluster by selectively activating specific internal modes depending on the mass distributions of the cluster.

While Sec. III and Sec. IV have focused on the transitions between PBP and COCT, we have also investigated other types of transitions of the LJ_7 cluster such as the transitions between COCT and IST in a similar manner to Sec. III. We have then observed a qualitative similarity between the roles played by the twist centrifugal forces in the transitions between COCT and IST and those in the transitions between COCT and PBP. This similarity has been as expected since IST and PBP have similar oblate mass distributions, and both the transitions between COCT and IST and those between COCT and PBP require a similar type of transformations of symmetry of mass distributions. This indicates that the symmetry breaking effect of the twist centrifugal forces could be of universal significance in the structural transitions between oblate and prolate isomers of molecules. On the other hand, characterizing the difference between the transitions from COCT to PBP and the transitions from COCT to IST would require more detailed quantitative analysis of the driving forces and energy transfers.

In the numerical experiments of selective activations of hyperspherical modes in Sec. IV, we have activated only two preselected modes by putting equal amount of kinetic energy. This has been to single out a small number of predominant modes in the structural transitions on an equal footing. For the sake of inducing structural transitions as rapidly as possible, on the other hand, it could be more efficient to activate more than two hyperspherical modes with appropriate partitioning of kinetic energy. Ideally, we expect that the partitioning of kinetic energy that resembles the one right before structural transitions observed in Fig. 9 is effective. It is thereby an interesting next step to search for an optimized way of activations of modes for an efficient control of structural transitions. It is also important to examine experimental feasibility of the selective activation of the hyperspherical modes. Since the gyration-radius modes are essentially the breathing modes along the three principal axes (see Fig. 4) and may often resemble the standard normal modes, it could be feasible to activate the gyration-radius modes. As for the activation of twisting modes, control of the movements of three principal axes of a molecule could be important since the twisting modes are directly coupled to the movements of principal axes via Eqs. (16)–(18).

The present study has indicated that gyration radii and principal axes can generally serve as useful collective variables for structural transitions of systems accompanying significant changes in the overall mass distributions as in the oblate-prolate transitions. As for local structural changes of systems with relatively small changes in the overall mass distributions, on the other hand, gyration radii and principal axes may not be able to characterize the structural changes clearly. However, one can still expect that, even for local structural changes of systems, the twist centrifugal forces as well as the shear centrifugal forces can be the dynamical driving forces in a similar manner to the present study. This is because these internal centrifugal forces can generally affect the movements of local structures by acting on the gyration radii of the overall system. Thus, the present method of hyperspherical modes would be interesting to apply not only to structural transitions accompanying significant changes in the overall mass distributions but also to localized structural changes for the exploration of driving forces.

Since oblate and prolate mass distributions are ubiquitous among interesting molecular systems of modern chemical physics, including fullerenes,[24–26] viral capsids,[27,28] and colloid clusters,[29–31] the driving mechanisms for oblate-prolate transitions presented in the present study could be of rather universal significance. For example, the symmetry breaking effect of the twist centrifugal forces shown in the present study could trigger dissociations and disruptions of symmetric molecular structures such as those of fullerenes and viral capsids. On the other hand, suppressing the twist centrifugal force could be important for the formation and stabilization of these symmetric structures. Since the twist centrifugal force tends to be very strong near symmetric structures, where two or three of the gyration radii are close to each other (see Sec. II D), we expect that the roles of the twist centrifugal force become extremely interesting and important in the dynamics near symmetric structures. It would also be an important next step to examine the significance of the effect of twist and shear centrifugal forces in the dynamics in thermal and noisy environments such as in the Langevin dynamics. Since these internal centrifugal forces are the dynamical forces originating from the coupling between gyration radii and twisting and shearing motions, their roles would generally become prominent in high-energy or high-temperature regimes. In this manner, extensions of the present study to more complex systems and to the systems in different environments could prove universal significance of the symmetry breaking effect arising in molecular internal dynamics.

ACKNOWLEDGMENTS

This work has been partially supported by JSPS Grants-in-Aid, Nos. 23740300 and 26800207, and by Waseda University Grant for SR 2012A-602.

[1]R. S. Berry, Chem. Rev. **93**, 2379 (1993).
[2]P. A. Braier, R. S. Berry, and D. J. Wales, J. Chem. Phys. **93**, 8745 (1990).
[3]D. Wales, *Energy Landscapes: Applications to Clusters, Biomolecules and Glasses* (Cambridge University Press, Cambridge, 2003).
[4]D. Chakrabarti, H. Kusumaatmaja, V. Ruhle, and D. J. Wales, Phys. Chem. Chem. Phys. **16**, 5014 (2014).
[5]J. Jellinek, T. L. Beck, and R. S. Berry, J. Chem. Phys. **84**, 2783 (1986).
[6]H. L. Davis, J. Jellinek, and R. S. Berry, J. Chem. Phys. **86**, 6456 (1987).
[7]P. Labastie and R. L. Whetten, Phys. Rev. Lett. **65**, 1567 (1990).
[8]M. Schmidt, R. Kusche, T. Hippler, J. Donges, W. Kronmüller, B. von Issendorff, and H. Haberland, Phys. Rev. Lett. **86**, 1191 (2001).
[9]F. Calvo and D. J. Wales, J. Chem. Phys. **128**, 154501 (2008).
[10]R. S. Berry and B. M. Smirnov, J. Chem. Phys. **130**, 064302 (2009).
[11]F. G. Amar and R. S. Berry, J. Chem. Phys. **85**, 5943 (1986).
[12]K. Takatsuka and C. Seko, J. Chem. Phys. **105**, 10356 (1996).
[13]C. Seko and K. Takatsuka, J. Chem. Phys. **108**, 4924 (1998).
[14]M. A. Miller and D. J. Wales, J. Chem. Phys. **107**, 8568 (1997).
[15]R. J. Hinde and R. S. Berry, J. Chem. Phys. **99**, 2942 (1993).
[16]T. Komatsuzaki and R. S. Berry, J. Chem. Phys. **110**, 9160 (1999).
[17]T. Komatsuzaki and R. S. Berry, J. Chem. Phys. **115**, 4105 (2001).
[18]J. Jellinek and D. H. Li, Phys. Rev. Lett. **62**, 241 (1989).
[19]F. Calvo and P. Parneix, J. Chem. Phys. **119**, 256 (2003).
[20]A. A. Rybakov, E. D. Belega, and D. N. Trubnikov, J. Chem. Phys. **133**, 144101 (2010).
[21]F. Calvo, Phys. Rev. E **87**, 022901 (2013).
[22]R. Ludwig, Angew. Chem., Int. Ed. **40**, 1808 (2001).

[23]C. Hock, M. Schmidt, R. Kuhnen, C. Bartels, L. Ma, H. Haberland, and B.v. Issendorff, Phys. Rev. Lett. **103**, 073401 (2009).
[24]V. R. Bhardwaj, P. B. Corkum, and D. M. Rayner, Phys. Rev. Lett. **91**, 203004 (2003).
[25]T. Laarmann, I. Shchatsinin, A. Stalmashonak, M. Boyle, N. Zhavoronkov, J. Handt, R. Schmidt, C. P. Schulz, and I. V. Hertel, Phys. Rev. Lett. **98**, 058302 (2007).
[26]N. Niitsu, M. Kikuchi, H. Ikeda, K. Yamazaki, M. Kanno, H. Kono, K. Mitsuke, M. Toda, and K. Nakai, J. Chem. Phys. **136**, 164304 (2012).
[27]D. J. Wales, Philos. Trans. R. Soc., A **363**, 357 (2005).
[28]M. F. Hagan and D. Chandler, Biophys. J. **91**, 42 (2006).
[29]V. N. Manoharan, M. T. Elsesser, and D. J. Pine, Science **301**, 483 (2003).
[30]G. Meng, N. Arkus, M. P. Brenner, and V. N. Manoharan, Science **327**, 560 (2010).
[31]D. Zerrouki, J. Baudry, D. Pine, P. Chaikin, and J. Bibette, Nature **455**, 380 (2008).
[32]G. Hummer and I. G. Kevrekidis, J. Chem. Phys. **118**, 10762 (2003).
[33]R. Elber, Curr. Opin. Struc. Biol. **15**, 151 (2005).
[34]W. H. Miller, N. C. Handy, and J. E. Adams, J. Chem. Phys. **72**, 99 (1980).
[35]C. Dellago, P. G. Bolhuis, F. S. Csajka, and D. Chandler, J. Chem. Phys. **108**, 1964 (1998).
[36]P. G. Bolhuis, D. Chandler, C. Dellago, and P. L. Geissler, Annu. Rev. Phys. Chem. **53**, 291 (2002).
[37]L. Maragliano, A. Fischer, E. Vanden-Eijnden, and G. Ciccotti, J. Chem. Phys. **125**, 024106 (2006).
[38]E. Vanden-Eijnden and M. Venturoli, J. Chem. Phys. **130**, 194103 (2009).
[39]D. J. Wales, Mol. Phys. **100**, 3285 (2002).
[40]D. J. Wales, Mol. Phys. **102**, 891 (2004).
[41]F. Noé and S. Fischer, Curr. Opin. Struct. Biol. **18**, 154 (2008).
[42]D. Prada-Gracia, J. Gómez-Gardeñes, P. Echenique, and F. Falo, PLoS Comput. Biol. **5**, e1000415 (2009).
[43]M. J. Davis and S. K. Gray, J. Chem. Phys. **84**, 5389 (1986).
[44]N. De Leon, M. A. Mehta, and R. Q. Topper, J. Chem. Phys. **94**, 8310 (1991).
[45]T. Uzer, C. Jaffé, J. Palacián, P. Yanguas, and S. Wiggins, Nonlinearity **15**, 957 (2002).
[46]F. Gabern, W. S. Koon, J. E. Marsden, and S. D. Ross, Physica D **211**, 391 (2005).
[47]H. Waalkens, R. Schubert, and S. Wiggins, Nonlinearity **21**, R1 (2008).
[48]C. Eckart, Phys. Rev. **46**, 383 (1934).
[49]X. Chapuisat and A. Nauts, Phys. Rev. A **44**, 1328 (1991).
[50]X. Chapuisat, Phys. Rev. A **45**, 4277 (1992).
[51]A. Kuppermann, Adv. Mol. Vib. Collision Dyn. **2B**, 117 (1993).
[52]A. Kuppermann, J. Phys. Chem. **100**, 2621 (1996).
[53]A. Kuppermann, J. Phys. Chem. A **101**, 6368 (1997).
[54]V. Aquilanti, A. Lombardi, and E. Yurtsever, Phys. Chem. Chem. Phys. **4**, 5040 (2002).
[55]V. Aquilanti, A. Lombardi, M. B. Sevryuk, and E. Yurtsever, Phys. Rev. Lett. **93**, 113402 (2004).
[56]V. Aquilanti, A. Lombardi, and M. B. Sevryuk, J. Chem. Phys. **121**, 5579 (2004).
[57]M. B. Sevryuk, A. Lombardi, and V. Aquilanti, Phys. Rev. A **72**, 033201 (2005).
[58]V. Aquilanti, A. Lombardi, and M. Sevryuk, Regular Chaotic Dyn. **19**, 318 (2014).
[59]C. Eckart, Phys. Rev. **47**, 552 (1935).
[60]M. Kummer, Indiana Univ. Math. J. **30**, 281 (1981).
[61]A. Guichardet, Ann. Inst. H. Poincaré Phys. Théor. **40**, 329 (1984).
[62]R. G. Littlejohn and M. Reinsch, Rev. Mod. Phys. **69**, 213 (1997).
[63]J. D. Louck and H. W. Galbraith, Rev. Mod. Phys. **48**, 69 (1976).
[64]J. E. Marsden and T. S. Ratiu, *Introduction to Mechanics and Symmetry* (Springer, New York, 1999).
[65]J. E. Marsden, T. S. Ratiu, and J. Scheurle, J. Math. Phys. **41**, 3379 (2000).
[66]A. Tachibana and T. Iwai, Phys. Rev. A **33**, 2262 (1986).
[67]T. Iwai, Ann. Inst. H. Poincaré Phys. Théor. **47**, 199 (1987).
[68]T. Yanao and K. Takatsuka, Phys. Rev. A **68**, 032714 (2003).
[69]T. Yanao and K. Takatsuka, J. Chem. Phys. **120**, 8924 (2004).
[70]T. Yanao, W. S. Koon, J. E. Marsden, and I. G. Kevrekidis, J. Chem. Phys. **126**, 124102 (2007).
[71]T. Yanao, W. S. Koon, and J. E. Marsden, J. Chem. Phys. **130**, 144111 (2009).
[72]T. Yanao, Y. Oka, and W. S. Koon, J. Therm. Sci. Technol. **8**, 423 (2013).
[73]E. W.-G. Diau, J. L. Herek, Z. H. Kim, and A. H. Zewail, Science **279**, 847 (1998).
[74]B. C. Dian, A. Longarte, and T. S. Zwier, Science **296**, 2369 (2002).
[75]D. R. Killelea, V. L. Campbell, N. S. Shuman, and A. L. Utz, Science **319**, 790 (2008).
[76]J. R. Fair, K. R. Wright, and J. S. Hutchinson, J. Phys. Chem. **99**, 14707 (1995).
[77]R. Mitrić, C. Bürgel, and V. Bonačić-Koutecký, Proc. Natl. Acad. Sci. U. S. A. **104**, 10314 (2007).
[78]P. Du Toit, I. Mezić, and J. E. Marsden, Physica D **238**, 490 (2009).
[79]W. S. Koon, H. Owhadi, M. Tao, and T. Yanao, Chaos **23**, 013117 (2013).
[80]J. C. Castro Palacio, L. Velazquez Abad, A. Lombardi, V. Aquilanti, and J. Rubayo Soneíra, J. Chem. Phys. **126**, 174701 (2007).
[81]J. C. Castro Palacio, J. Rubayo-Soneíra, A. Lombardi, and V. Aquilanti, Int. J. Quantum Chem. **108**, 1821 (2008).